

$1/\omega$ electric-field noise in surface ion traps from correlated adsorbate dynamics

Benjamin L. Foulon¹, Keith G. Ray,² Chang-Eun Kim,² Yuan Liu,³ Brenda M. Rubenstein^{4,*}, and Vincenzo Lordi^{2,*}

¹*Department of Chemical Engineering, Brown University, Providence, Rhode Island 02912, USA*

²*Quantum Simulations Group, Lawrence Livermore National Laboratory, Livermore, California 94550, USA*

³*Center for Ultracold Atoms, Research Laboratory of Electronics, Massachusetts Institute of Technology, Cambridge, Massachusetts 02139, USA*

⁴*Department of Chemistry, Brown University, Providence, Rhode Island 02912, USA*



(Received 2 July 2021; accepted 3 January 2022; published 19 January 2022)

Ion traps are promising architectures for implementing quantum computers, but they suffer from excessive “anomalous” ion motional heating that limit their overall coherence and practicality for scalable quantum computing. The exact microscopic origins of anomalous heating remain an open question, but experiments point to adsorbates on trap electrodes as one likely source. Many different models of anomalous heating have been proposed, but these models have yet to pinpoint the atomistic origin of the experimentally observed $1/\omega$ electric-field noise scaling seen in ion traps at frequencies between 0.1–10 MHz. In this work, we show that a model based on previously proposed surface-induced dipole fluctuations on adsorbates, but which also incorporates interparticle interaction dynamics through molecular dynamics simulations of up to multiple monolayers of adsorbates, gives rise to $1/\omega$ frequency scaling at the MHz frequencies typically employed in ion traps. These results demonstrate that moderate-to-high densities of adsorbates can give rise to a set of activated motions that produce the $1/\omega$ noise observed in ion traps and that collective adsorbate motions produce the observed noise spectra that a noninteracting model does not capture.

DOI: [10.1103/PhysRevA.105.013107](https://doi.org/10.1103/PhysRevA.105.013107)

I. INTRODUCTION

Fault-tolerant quantum computers capable of scaling to many qubits have outstanding potential to impact many fields of science and technology but remain beyond our current grasp, in large part due to noise [1]. One particularly pernicious and ubiquitous form of noise that limits the coherence times of trapped ion [2–5], superconducting qubit [6–8], Rydberg atom [9], nitrogen-vacancy-center based [10], and many other quantum architectures is surface noise. In ion traps, surface-derived electric-field noise has long been known to limit the fidelity of quantum gates by exciting (“heating”) the very ion motional modes upon which these gates depend [4]. The exact microscopic source of this electric-field noise, however, remains far less understood. Intuition might suggest that Johnson noise [11,12] could be the dominant source of noise, or at least its ultimate lower bound, but a number of researchers have independently shown that a different, still unknown, and therefore “anomalous” source of noise dominates the observed heating rates in ion traps and is typically orders of magnitude higher than expected for Johnson noise [5,13]. The origin of this noise thus remains an open question, whose solution would lead to dramatically improved performance of ion trap-based quantum information processors [14–16], sensors [17–20], and clocks [21–23].

Experiments directed at characterizing noise have revealed that the three key parameters that control the electric-field

noise, S_E , are the distance at which the ion is trapped above the electrode surface d , the trapping frequency ω , and the trap temperature T , such that

$$S_E \propto \omega^{-\alpha} d^{-\beta} f(T), \quad (1)$$

where $f(T)$ is a function of the temperature [4]. Although aspects of this functional form and its exponents are still a subject of debate [4,24], most experiments point to a frequency scaling exhibiting $\alpha \sim 1$ at MHz frequencies [3,25–29]. Many of these same experiments also suggest a distance scaling of d^{-4} with $\beta = 4$ [3,25–27,29–31], which stands in stark contrast with Johnson noise, which scales as d^{-2} .

Over the past decade, a number of different microscopic models [28,32,33] have been advanced that aim to both reproduce and explain these scalings, which serve as useful constraints on the possible mechanisms that could give rise to anomalous heating. One of the earliest models proposed was the patch potential model [3], which espouses that local variations of electrode potentials can induce ion motion with the d^{-4} noise scaling observed in experiments. The patch potential model, however, does not identify the source of the local fluctuations on which it is based. In light of experiments demonstrating that different treatments that remove surface adsorbates, including ion milling [34–36], plasma treatment [37], and laser cleaning [38], reduced trap noise by up to two orders of magnitude, it is logical to attribute this noise to dipole fluctuations caused by adsorbates bound to trap electrodes.

*These authors contributed equally to this work.

Along these lines, two particularly compelling noise models are the adatom dipole and diffusion models. The adatom dipole model posits that atoms and molecules that adsorb onto electrode surfaces to form layers or patches develop induced dipole moments that locally lower the work function, and therefore the potential, of the metal [4,39]. The dipoles may then be caused to fluctuate by phonon-induced transitions among different vibrational states of the adatom-surface potential, giving rise to the requisite fluctuation spectra. Initial investigations of this model that treated noninteracting adsorbates using plausible values for their masses and forms for their binding potentials illustrated that it can differentiate the effects of different adsorbates but yielded electric-field noise spectra that are considerably lower in magnitude to those observed in experiments [39–41]. In addition, for realistic parameters, the predicted spectra are flat as a function of frequency at low frequencies (the “white-noise” regime) and transition to decaying as $1/\omega^2$ at high frequencies with only a narrow band of $1/\omega$ dependence in-between. They also exhibit a large discrepancy in the frequency at which this turning point occurs, which is much higher than observed in experiments. Such behavior is consistent with two-level fluctuator models prevalent in the signal processing literature [42–44].

More recent work employing a first-principles treatment of noninteracting hydrocarbon, water, and other adsorbate binding potentials and dipole moments similarly exhibited a narrow $1/\omega$ region in its predicted spectra, but at very high frequencies inconsistent with experiments [41]. That work additionally included in-plane adsorbate vibrations, which produced the highest electric-field noise and exhibited $1/\omega$ scaling at lower frequencies and over a larger frequency range; however, these frequencies were still orders of magnitude larger than the typical 1-MHz trap frequency.

In the adatom diffusion model, dipole fluctuations are instead viewed as originating from the diffusion of an adatom or adsorbate across the surface of an electrode [45]. Noninteracting adatoms diffusing over a surface covered with patches having different work functions may be shown to produce fluctuation spectra that scale as $\omega^{-1.5}$. However, previous studies have not considered the effects of coupled diffusion and vibration; in particular, they have not accounted for the interplay of the corrugated potentials in the plane of the surface on the dipole dynamics of interacting adsorbates.

Even though the models described above do not produce extended regions with $1/\omega$ frequency scalings in their current forms, the inclusion of realistic features such as adatom-adatom interactions and surface corrugation may lead to more complicated spectral features that have yet to be illuminated or understood. This thus raises the question of whether a more realistic treatment of adatom dipole fluctuations that incorporates diffusion and interparticle interactions may exhibit the so far *theoretically elusive* $1/\omega$ scaling expected from experiments.

In this work, we examine the frequency dependence of the electric-field fluctuation spectra produced by the dynamics of up to multiple monolayers of interacting adsorbates on a surface. To study the adsorbate dynamics, we modeled them using classical molecular dynamics (MD) on potential energy surfaces (PES) constructed based on first-principles density functional theory (DFT) calculations. From the MD tra-

jectories, we obtained coverage- and temperature-dependent dipole-dipole fluctuation spectra using DFT-derived dipole moments. This enables us to make a clear connection between the features of the fluctuation spectra at different frequencies and the underlying adsorbate motions that give rise to these features. Here, we use methane on gold as a model system; this is a logical extension from earlier theoretical and experimental studies done on work function changes in carbon-gold systems [46], and it provides a way to compare to previous detailed results that only looked at noninteracting cases. It is also a step towards representing hydrocarbon molecules that may be present on the electrodes of fabricated ion traps; the particular parameters of the model can be varied to represent other surfaces and adsorbates consistent with specific experimental conditions.

We find that correlated dipole fluctuations from the interacting adsorbate dynamics produce $1/\omega$ noise spectra with larger magnitudes than the noninteracting case, much more consistent with observed behavior, by only adding the adsorbate-adsorbate interactions to the model and not changing the underlying physics of induced dipole fluctuations. We identify several key microscopic motions that naturally lead to the $1/\omega$ frequency scaling in the MHz regime used in most ion traps. In particular, we find that correlated rotational and translational motions of adsorbates within clusters can give rise to $1/\omega$ electric-field noise at submonolayer coverages, while interlayer particle exchanges among the first two layers of adsorbates are the largest contributors to such noise at supermonolayer coverages. We furthermore show how many of the MHz features of the electric-field spectra for these systems may be reproduced by a two-level fluctuator model with these motions as rare events. Even though the methane-gold system we study here is a model system that contains simplifications, our work provides clear evidence for the types of adsorbate motions that can give rise to anomalous heating and demonstrates the crucial role that collective, rather than individual, adsorbate motions assume in the noise generation process at experimental trap frequencies.

This paper is organized as follows. In Sec. II, we begin by describing how we model the dipole-dipole fluctuation spectra of methane on a gold substrate using our combined DFT-MD approach. We next describe our results, including our key findings regarding the $1/\omega$ to $1/\omega^2$ frequency dependence of the dipole-dipole fluctuation spectra we obtain for varying adsorbate surface coverages and temperatures in Sec. III. In the same section, we additionally present our data directly linking specific adsorbate motions with features of the frequency spectra and demonstrate how our spectra can be reproduced using simple two-state models. Lastly, in Sec. IV, we place our findings that a realistic model of multilayer adsorbate dynamics can give rise to $1/\omega$ noise in the context of the ongoing search for the microscopic origins of anomalous heating, and discuss the limitations and natural extensions of our current model. Additional information regarding our simulations and interpretation of the data may be found in the Appendices.

II. METHODS

In this work, we model methane adsorbate dynamics on gold substrates at a range of temperatures and

surface coverages by running classical MD trajectories on a DFT-derived substrate potential energy surface (PES). Based upon the trajectories obtained, we then compute adsorbate dipole-dipole correlation functions and Fourier transform them to acquire dipole-dipole fluctuation spectra. These spectra are subsequently analyzed for their frequency-dependent behavior, which can be used to predict electric-field noise and ion trap heating rates.

A. Calculation of heating rates

As has been shown in previous work [3], the coupling of electric-field fluctuations with the motion of trapped ions gives rise to a heating rate \dot{n} , that is given by

$$\dot{n} = \frac{q^2}{4m_I\hbar\omega_t} S_E(\omega_t). \quad (2)$$

Here, q is the charge of the ion, m_I is the mass of the ion, ω_t is the frequency at which the ion is trapped (typically 0.1–10 MHz), and \hbar is the reduced Planck's constant. $S_E(\omega)$ is the frequency spectrum of the electric-field fluctuations. Patch potential models assert that electric-field noise in traps stems from local potential fluctuations above the surfaces of the electrodes [4,47,48]. These fluctuations can arise from regions of the electrodes with varying crystal orientations or adsorbate surface motion. In the latter case, which is the focus of this investigation, fluctuations in the dipole moment of the adsorbates caused by electronic interactions with the electrode surface give rise to electric-field noise. Specifically, for a conventional planar trap [4], $S_E(\omega)$ may be obtained from out-of-plane adsorbate dipole fluctuations in a surface patch by [41]

$$S_E(\omega) = \frac{3\pi\sigma S_\mu(\omega)}{2(4\pi\epsilon_0)^2 d^4} \quad (3)$$

and from in-plane fluctuations by

$$S_E(\omega) = \frac{\pi\sigma S_\mu(\omega)}{(4\pi\epsilon_0)^2 d^4}. \quad (4)$$

In Eqs. (3) and (4), σ is the average area density of the surface patches, d is the ion-electrode distance, ϵ_0 is the permittivity of free space, and $S_\mu(\omega)$ is the dipole-dipole fluctuation spectrum. Notably, these expressions for $S_E(\omega)$ reflect the d^{-4} scaling that has often been observed experimentally in heating rates and is one key reason why we and others continue to examine this model.

The dipole-dipole fluctuation spectrum of a surface patch can be calculated by taking the Fourier transform of the dipole-dipole autocorrelation function

$$S_\mu(\omega) = \int_{-\infty}^{+\infty} d\tau e^{i\omega\tau} C_{\mu,\mu}(\tau), \quad (5)$$

where $C_{\mu,\mu}(\tau)$ represents the dipole-dipole autocorrelation function of the total patch dipole moment at time τ . This autocorrelation function may be expressed as

$$C_{\mu,\mu}(\tau) = \langle [\mu_z(\tau) - \langle \mu_z \rangle][\mu_z(0) - \langle \mu_z \rangle] \rangle = \langle \Delta\mu_z(\tau)\Delta\mu_z(0) \rangle. \quad (6)$$

In the above, $\mu_z(\tau)$ is the z component of the total dipole moment of a patch at time τ and $\langle \mu_z \rangle$ is its equilibrium

average. Although a full treatment would use $\vec{\mu}$, we instead use μ_z unless otherwise specified. The values of the x and y components of our adsorbate dipoles are orders of magnitude smaller than the z components. There are only a small handful of cases where the x or y components would affect spectra generated by z components alone (see Appendix G).

In this work, we assume that $C_{\mu,\mu}(\tau)$ stems from how the dipole moments of N different adsorbates change as they move across a surface with a spatially varying binding potential. The quantity $\Delta\mu_z(\tau)$ represents a fluctuation of the electric dipole moment of the simulation cell, which is a sum over the individual adsorbate dipole fluctuations. This definition remains valid for Eqs. (3) and (4) as long as the simulation cell is small compared to the ion-electrode distance d , and it captures the effect of adsorbate correlations on the noise as long as the simulation cell is larger than the correlation length [4]. The first condition is satisfied as the typical ion-electrode distance is 40 μm and the simulation cell dimensions are less than 100 nm. The adsorbate-adsorbate correlation length is shown to be smaller than the simulation size in Sec. III B.

In this limit, we may express the surface patch dipole-dipole correlation function in terms of the adsorbate dipole fluctuations as

$$\begin{aligned} C_{\mu,\mu}(\tau) &= \left\langle \sum_i^N \Delta\mu_{i,z}(\tau) \sum_j^N \Delta\mu_{j,z}(0) \right\rangle \\ &= \left\langle \sum_{i,j}^{N,N} \Delta\mu_{i,z}(\tau) \Delta\mu_{j,z}(0) \right\rangle \\ &\quad + \left\langle \sum_{i,j}^{N,N} \Delta\mu_{i,z}(\tau) \Delta\mu_{j,z}(0) \right\rangle_{i \neq j}, \end{aligned} \quad (7)$$

where $\Delta\mu_{i,z}(\tau)$ represents the fluctuation of the z component of the electric dipole moment of adsorbate i at time τ . In the last expression, we have divided the sum into a sum over dipole-dipole correlation functions of the individual ($i = j$) adsorbates and a sum over those correlations between distinct ($i \neq j$) adsorbates. If there were no correlation between different adsorbates, the second term would vanish. We calculate both of these sums and demonstrate the importance of dipole-dipole correlations between different adsorbates in Sec. III B.

In practice, we evaluate Eq. (6) by averaging over all of the individual adsorbate dipole-dipole autocorrelation functions taken across the entire simulation run time \mathcal{T} :

$$C_{\mu,\mu}(\tau) = \frac{1}{(\mathcal{T} - \tau)} \sum_{k=1}^{\mathcal{T}-\tau} \left[\sum_i^N \Delta\mu_{i,z}(\tau + t_k) \sum_j^N \Delta\mu_{j,z}(t_k) \right], \quad (8)$$

where $\mathcal{T} - \tau$ denotes the number of time steps taken between these two times.

B. Generation of the electrode potential energy surface

In order to calculate the fluctuations of the dipole moments required by Eq. (8), a PES of CH₄ physisorbed onto Au(111) was interpolated from DFT CH₄-Au(111) binding energies

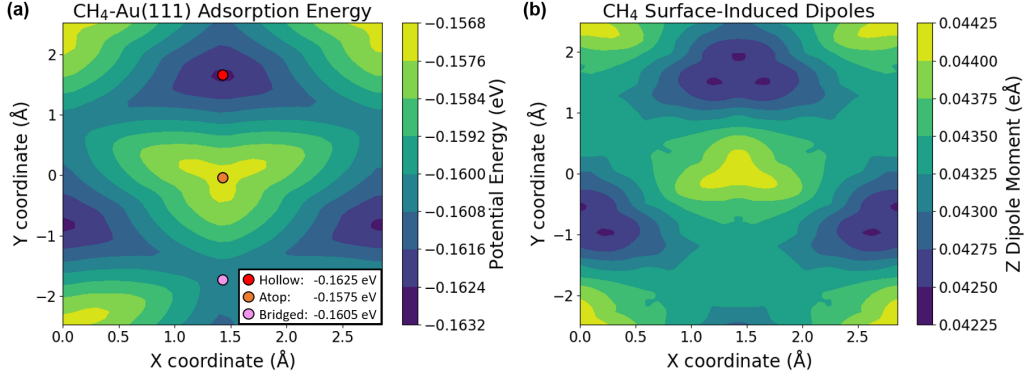


FIG. 1. Visualization of the CH₄-Au(111) potential energy surface generated from DFT calculations spanning one Au(111) unit cell at an adsorbate-surface distance of 3.16 Å, which is the minimum-energy, out-of-plane distance. The red (dark), orange (medium), and pink (light) circles designate the positions of the Au(111) hollow, atop, and bridged sites, respectively. (b) Visualization of the magnitudes of the surface-induced methane dipole moments as a function of methane position in the same Au(111) cell and at the same height as on the left.

taken at a representative set of positions on the Au(111) surface. In all of our simulations, the methane adsorbates were treated as point particles, a reasonable simplification given their spherical character, and we did not consider the effects of phonons.

The DFT calculations were performed with VASP [49] using the vdW-DF-cx functional [50] at a single k point and a plane-wave cutoff of 600 eV. The resulting potential energy points were interpolated across a periodic surface. The interpolated PES employed has dimensions of 2.856, 4.947, and 29.0 Å in the x , y , and z directions, respectively. Figure 1(a) depicts this PES in the (x , y) plane for one Au(111) unit cell at the minimum-energy distance from the carbon of the adsorbate to the surface of 3.16 Å. The simulation cell contained 72 such unit cells (12 in the x direction and 6 in the y direction). This unit-cell tiling was chosen so as to make the dimensions of the overall simulation cell roughly the same in both the x and y directions to reduce any spurious adsorbate ordering effects from anisotropic boundary conditions. As can be seen in Fig. 1(a), the hollow site marks the lowest-energy binding position on this surface (-0.1625 eV), while the atop site marks the highest-energy position (-0.1575 eV). Additional simulation parameters may be found in Table I, and additional binding energies at different positions on the surface may be found in Table 5. In addition to the surface-adsorbate interaction, each adsorbate was modeled as interacting with its neighbors through the methane-methane optimized potentials

for liquid simulations (OPLS) potential [51] such that

$$V_{\text{adsorbate}} = V_{\text{surface}} + V_{\text{interparticle}}, \quad (9)$$

where

$$V_{\text{interparticle}} = 4\epsilon_{\text{CH}_4} \left[\left(\frac{\sigma_{\text{CH}_4}}{r_{ij}} \right)^{12} - \left(\frac{\sigma_{\text{CH}_4}}{r_{ij}} \right)^6 \right]. \quad (10)$$

In this equation, ϵ_{CH_4} denotes the OPLS CH₄-CH₄ interaction energy, while σ_{CH_4} denotes the CH₄-CH₄ interaction radius. r_{ij} represents the interparticle distance between the centers of mass of methanes i and j . Based upon the OPLS interaction radius, the methanes would prefer to be spaced 4.19 Å from one another. As we will see, this spacing favored by the OPLS potential competes with the particle spacing favored by the surface potential to produce different particle surface configurations at different temperatures, which in turn give rise to the different types of particle motions that are reflected in the dipole-dipole fluctuation spectra.

C. Molecular dynamics using the atomic simulation environment

The atomic simulation environment (ASE) was used to perform the MD simulations with the interpolated CH₄-Au(111) and OPLS potentials. Running MD simulations based upon this interpolated landscape is much more computationally efficient than running fully *ab initio* simulations and is therefore key to reaching the timescales required to observe events happening in the 0.1–10 MHz frequency range at which ions are trapped.

ASE is an open-source software platform for atomistic simulations [52]. It is also Python based, which makes it possible to seamlessly incorporate the Python-interpolated PES directly into the MD setup. The MD scripts used can be found in this paper's Github repository [53].

NVT MD simulations were performed using Langevin dynamics with a friction coefficient of 0.01 atomic units (a.u., where 1 a.u. = 4.13×10^{16} s⁻¹). Particle forces and energies were updated every 5 fs, and positions were recorded for analysis every 1 ps to ensure that configurations were not artificially correlated. These parameters were verified to be computationally efficient while providing comparable system

TABLE I. Simulation details and parameters.

CH ₄ -Au(111) potential	DFT, vdW-DF-cx
CH ₄ -Au(111) min. energy distance	3.16 Å
CH ₄ -Au(111) min. energy	-0.1625 eV
OPLS min. energy distance	4.19 Å
σ_{CH_4} for OPLS	3.73 Å
ϵ_{CH_4} for OPLS	0.01275 eV
MD environment	ASE
Thermostat	Langevin
Friction coefficient	4.13×10^{16} s ⁻¹
MD force update step	5 fs
MD position recording step	1 ps

equilibration and dynamics to those obtained using smaller friction coefficients and step sizes. In order to isolate collective motions of interest from thermostat-induced cluster translations and drifts, the thermostat was configured to fix the center-of-mass position and zero the center-of-mass momentum. Simulation run times ranged from 6 to 19 μ s for different sets of coverages (see the Appendix B). The MD simulation cell employed periodic boundary conditions in the x and y directions, but not in the z direction.

D. Calculation of dipole moments

The electric dipole moments of the methanes adsorbed over a range of positions on the gold surface were also computed with DFT using VASP. In particular, we integrated the charge density \times position, $\rho(r) \times r$, over a $40 \times 33.6 \times 29.1$ Å³ simulation cell containing an Au slab “island” with a finite extent in the in-plane directions and a single CH₄ molecule on top. A finite slab is required so that, if the adsorbate is moved within one Au surface unit, charge is not induced to move across the periodic boundaries and the integral remains well defined. The slab island consists of a 4×4 arrangement of Au surface primitive cells.

To map the surface-induced dipole moments as depicted in Fig. 1(b), we calculated the dipole moments for CH₄ at the surface positions illustrated in one surface unit cell located in the center of this slab and at varying heights. Electric dipole corrections were utilized in VASP and a small linear ramp in the dipole moment was subtracted to remove remaining finite-size effects and ensure that the dipole moment is periodic with respect to the surface in-plane periodicity. As in Sec. II B, these calculations were also performed using the vdW-DF-cx functional at a single k point and with a 600-eV plane-wave cutoff.

The resulting dipole moments were interpolated using an interpolation script to yield the x , y , and z components of the dipole vector as a function of an adsorbate’s position. The values of the x and y components of the dipole moments are negligible compared to the z -component values across the entire periodic cell, and their fluctuations do not produce much noise except in a handful of cases. Thus, we chose to make use of the z components of the dipole moments for the rest of this study.

A visualization of the z dipole moment surface at the minimum-energy out-of-plane surface-adsorbate distance can be found in Fig. 1(b). Comparing the dipole moment surface with the PES, it can be seen that the largest induced dipole moments occur at the locations with the largest potential energies, and vice versa. The dipole interpolation script that produced this surface is provided in this paper’s Github repository [53].

E. Dipole-dipole fluctuation spectra

Dipole-dipole autocorrelation functions were computed using Eq. (8) based upon how the adsorbate dipole moments change in time as they traverse the potential surface. As we modeled systems with varying surface coverages (see Table II), the exact value of N used in this equation depended upon the coverage studied. The first 1000 time steps (spanning 1 ns) were omitted to allow for equilibration. Dipole-dipole

TABLE II. Table of coverages and temperatures at which simulations were performed in this work.

Type	Coverage (N_{CH_4})
Submonolayer	0.36 ML (25)
Submonolayer	0.52 ML (36)
Submonolayer	0.71 ML (49)
Monolayer	1.0 ML (69)
Supermonolayer	1.16 ML (80)
Supermonolayer	1.42 ML (98)
Supermonolayer	1.86 ML (128)
Temp. < 70 K	20, 25, 30, 35, 40, 45, 50, 55, 60
Temp. ≥ 70 K	70, 80, 90, 100, 110, 125, 150, 184, 220

fluctuation spectra were then calculated by applying a discrete fast Fourier transform [54] to these correlation functions [per Eq. (5)]. A standard smoothing technique, Blackman smoothing [55], was applied before plotting.

F. Two-level fluctuators as a source of $1/\omega^2$ and $1/\omega$ noise

As will be discussed below, many of our fluctuation spectra demonstrate two-level fluctuator (TLF) or multilevel fluctuator behavior. A TLF is a system that transitions between two distinct states that are characterized by properties that can assume two distinct values. A TLF that switches between states 0 and 1 with properties differing in value by ΔI and that has mean state residence times of τ_0 and τ_1 will yield noise spectra of the following Lorentzian form [56]:

$$S(\omega) = \frac{4(\Delta I)^2}{(\tau_0 + \tau_1)[(1/\tau_0 + 1/\tau_1)^2 + \omega^2]}. \quad (11)$$

TLFs have a region of $1/\omega^2$ frequency scaling and a section of $1/\omega$ and near- $1/\omega$ scaling as the $1/\omega^2$ rounds off to white noise at the lowest frequencies. Moreover, ensembles of TLFs or multilevel fluctuators can produce $1/\omega$ regions [43]. For additional detail on TLFs, see Appendix D.

III. RESULTS AND DISCUSSION

A. Adsorbate-surface geometries

We begin by analyzing the geometries that the adsorbates assume at the different surface coverages studied. Because of the competing influences of the interparticle and surface-adsorbate potentials, the geometries are not straightforward to predict. Here, we visualize and discuss several emblematic coverages.

Within the simulation box employed in this work, we find that 69 adsorbates produce the full monolayer (ML) surface coverage with the lowest energy per adsorbate (see Fig. 15). We thus define our runs in terms of ($N/69$) ML coverages. In Fig. 2, for example, the 0.36-ML coverage on the left has 25 particles, whereas the 1.86-ML coverage on the right has 128 particles. As a guide to our subsequent discussion, we list all of the surface coverages and temperatures at which our simulations were performed in Table II. Figure 2(a) depicts a representative surface geometry of the 0.36-ML trajectory at 20 K. At this coverage, the methanes cluster together and

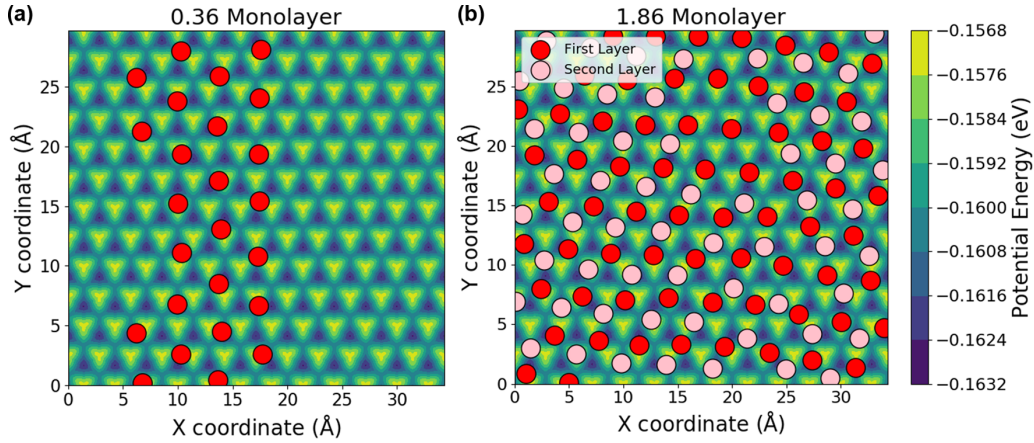


FIG. 2. Representative snapshots of the positions of the adsorbates on the Au(111) surface at 20 K for (a) 0.36-ML and (b) 1.86-ML coverages. Note that the intermolecular potential is stronger than the in-plane Au(111)-CH₄ potential barriers when the particles are near the surface. Because the adsorbates cannot simultaneously reside in the differing minima of their intermolecular and surface-adsorbate potentials, they do not all occupy lowest-energy hollow sites on the surface; instead, they organize into a more complicated, but repeating pattern. First-layer particles can have a maximum of six first-layer and three second-layer neighbors.

simultaneously try to minimize their interparticle energies while residing in the hollow-site minima of the Au(111) surface. Notably, the methanes cannot reside at every available hollow site because such sites are separated by only 2.856 Å, which is significantly less than $\sigma_{\text{CH}_4} = 3.73$ Å, the zero-energy OPLS distance. Since the OPLS well depth is greater than any surface site energy differences (see Tables I and V), the methanes occasionally settle for bridged or even atop sites in order to minimize interparticle repulsions. In so doing, they maintain a CH₄-CH₄ distance of >3.73 Å and close to the interparticle potential minimum-energy distance of 4.19 Å.

Habitually, the methanes lying near atop sites get pulled toward hollow sites and push neighboring hollow-site methanes into less favorable sites, and so on and so forth throughout the clusters. This in-plane rattling occurs often, within an extent of 1–2 Å and at much higher frequencies than trapped ion frequencies, but does not disrupt the cohesion of the clusters at low temperatures.

The methanes can also become perturbed enough to undergo more significant individual and collective movements, and while these significantly affect the noise spectra (see Sec. III C), they do not prevent the surface clusters from remaining intact and mostly stationary at low temperatures. At higher temperatures, the particles have plenty of thermal energy to leave both the surface and CH₄-CH₄ interaction wells, resulting in a more fluid and less-defined surface configuration.

Although most previous works have focused on adsorbate dynamics at submonolayer coverages assuming that diffusion across the electrode surface is the dominant source of noise [45], here we additionally examine supermonolayer adsorbate dynamics. Studying multiple monolayers is more true to experimental reality, as several experiments have shown multiple hydrocarbon monolayers to be present on untreated gold traps [34,45]. Figure 2(b) depicts a representative 1.86-ML bilayer coverage at 20 K. Not surprisingly, the second layer stacks on top of the first such that each second-layer particle is roughly equidistant [in the (x, y) plane] from its three

nearest first-layer neighbors, while typically staying at least 3.4–3.6 Å above the first layer (6.56–6.76 Å above the surface) in the z direction. This leads to clustering in the second layer, similar to how clusters formed on the surface at submonolayer coverages.

Second-layer clusters are affected by interparticle interactions from both first- and second-layer particles, but second-layer particles are not as strongly affected by the surface potential. In fact, at typical second-layer distances from the surface, the magnitude of the adsorbate-surface potential is comparable to the minimum OPLS energy. Beginning around 70 K, the second-layer clusters become less coherent as interparticle interactions become less restrictive to particle motion. This leads to more fluid second-layer particles, both parallel and perpendicular to the surface, some of which begin to stochastically exchange layers. Such exchanges can be reciprocal or unidirectional; in the latter case, the population of the surface changes. Although 69-adsorbate surfaces are slightly favored in monolayer conditions, other surface populations can manifest in supermonolayer coverages, including 68- and 70-adsorbate surfaces (see the Appendix C). As we will see in Sec. III D, the switching between different surface populations will become important in our interpretation of the dipole-dipole fluctuation spectra.

Due to the dwindling influence of the surface-electrode potential at further distances from the electrode surface, the propensity to form a cohesive third layer is significantly reduced. In addition, the dwindling electrode-adsorbate interaction strength makes it more difficult to keep weakly held second-layer particles from getting pushed up or drifting to higher surface heights as the second layer gets more crowded. For these reasons, we limit our focus to a maximum coverage of 1.86 ML. More visualizations of and information about different coverages can be found in the Appendix C.

B. Effects of correlated adsorbate motion on fluctuation spectra

To demonstrate the role that dipole-dipole correlations between distinct surface adsorbates play in the generation of the

electric-field noise affecting trapped ions, we decompose the total simulation patch dipole-dipole correlation spectrum into contributions from individual adsorbates and from distinct adsorbate pairs. This decomposition is expressed in Eq. (7) and presented in Fig. 3 for the case of a 0.52-ML coverage of adsorbed CH₄ at 30 K. The trends shown are representative of those also observed for different coverages and temperatures. We notice in Fig. 3(a) that, while the individual adsorbate dipole-dipole spectrum and the distinct adsorbate dipole-dipole spectrum both exhibit roughly a white-noise spectrum up to 10 MHz, the total dipole-dipole correlation spectrum scales as $1/\omega$ beyond 10 MHz. Therefore, capturing dipole-dipole correlations between distinct adsorbates is essential for reproducing the $1/\omega$ electric-field noise measured experimentally at frequencies of a few MHz.

Interestingly, the magnitude of the total dipole-dipole spectrum is smaller than that of either the individual or distinct pair adsorbate contributions. This occurs because the pair adsorbate dipole spectrum is close to the individual adsorbate dipole spectrum in magnitude, but is roughly π phase shifted and thus partially cancels the noise from the individual adsorbate dipole spectrum. In Fig. 3(b), we investigate this behavior in more detail by plotting the average spectrum of an individual adsorbate along with the dipole spectra between adsorbates that are nearest and next-nearest neighbors, corresponding to adsorbate separations of less than 6.0 Å and 6.0–9.0 Å, respectively. Positions were averaged over a window of 2000 time steps prior to spectral calculation. The colors of the plotted pair spectra indicate the phase as $\cos(\phi)$, with dark blue signifying $\cos(\phi) = -1$, $\phi = \pi$ and dark red indicating $\cos(\phi) = 1$, $\phi = 0$. Both the magnitude of the spectrum and its color are indicative of the correlation with the individual adsorbate dipole fluctuation. Nearest-neighbor dipoles are slightly anticorrelated on average, indicated by the dark blue color and a magnitude that is smaller than that of the individual adsorbate spectrum, while next-nearest neighbors have an even smaller correlation that is positive on average. While the magnitude of the dipole-dipole spectrum of an average nearest-neighbor pair is less than that of the individual adsorbate spectrum, there are 5.3 nearest neighbors on average for this coverage at this temperature, so the sum of all distinct pairs produces the dashed curve in Fig. 3(a).

In Fig. 3(c), we plot $\cos(\phi)S(\omega = 3.5 \text{ MHz})$ vs the distance between adsorbates i and j . From this plot, we can see how the magnitude and phase of the pair dipole-dipole fluctuation spectra evolve with separation. As above, ϕ is the phase difference between the distinct i/j adsorbate spectrum and the individual adsorbate spectrum; $\cos(\phi) = -1$ signifies anticorrelated adsorbate dipole fluctuations and $\cos(\phi) = 1$ signifies correlated adsorbate dipole fluctuations; and adsorbate positions were averaged over a window of 2000 time steps. In Fig. 3(c), we again see the anticorrelation of the nearest-neighbor adsorbates, which is strongest at 2.5 Å [see also the blue line in Fig. 3(b)]. We note, however, that most nearest-neighbor adsorbates are close to 4.5 Å apart, a distance at which the anticorrelation is weaker than at 2.5 Å. We can quantify the correlation between adsorbates as close as an angstrom or two apart because we average over many adsorbate configurations and a few such rare configurations arise given enough sampling. The correlation of the next-nearest

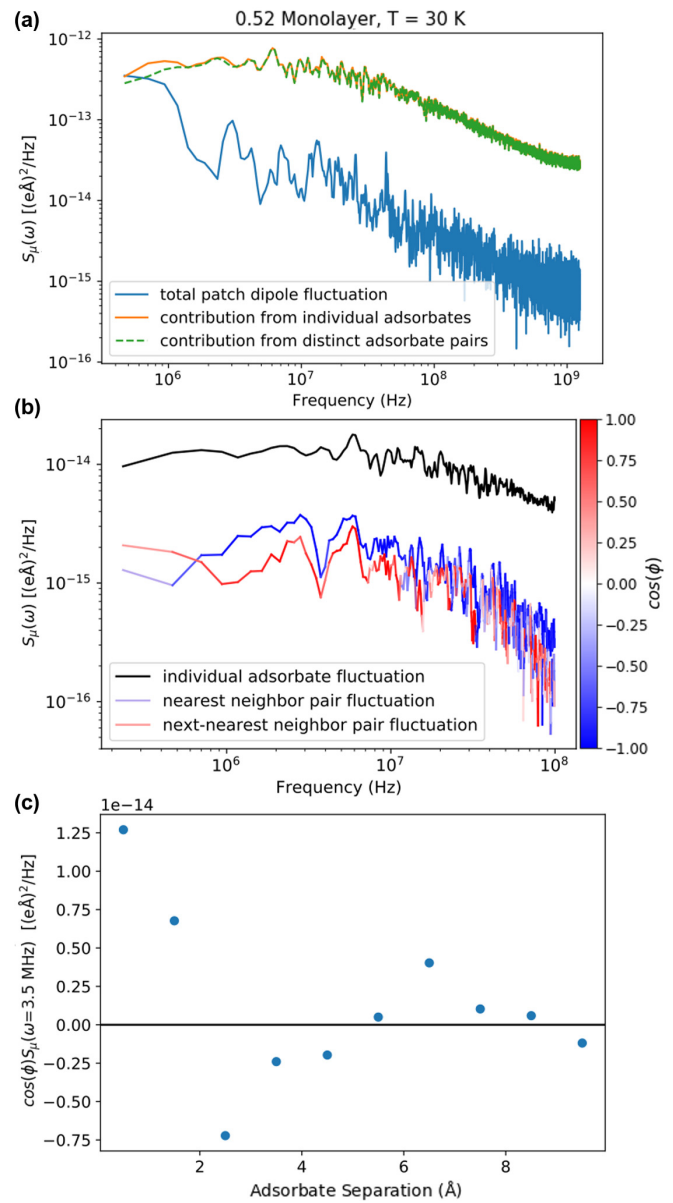


FIG. 3. (a) Patch total dipole fluctuation spectrum $S_\mu(\omega)$ in blue (bottom curve), and that spectrum decomposed into individual, orange ($i = j$), and distinct, dashed green ($i \neq j$) adsorbate contributions [per Eq. (7)], which significantly cancel each other. (b) Dipole-dipole fluctuation spectrum of an individual adsorbate, black line (top curve), and the spectra of pairs of adsorbates separated by less than 6.0 Å (middle curve), mostly blue, and between 6.0 to 9.0 Å (bottom curve), mostly red, corresponding to surface-adsorbate nearest neighbors and next-nearest neighbors. The colors of the nearest-neighbor and next-nearest-neighbor pair spectra are indicative of their relative phase compared to the individual adsorbate fluctuations, with $\cos(\phi) = 1(-1)$ being dark red (blue). ϕ is the phase difference between the distinct i/j adsorbate spectrum and the individual adsorbate spectrum at that frequency. (c) $\cos(\phi)S(\omega = 3.5 \text{ MHz})$ vs distance between adsorbates i and j .

neighbors, first captured by the red line in Fig. 3(b), is positive and most next-nearest-neighbor adsorbates are around 8 Å apart. We estimate the correlation length to be 5.7 Å, much smaller than our simulation cell.

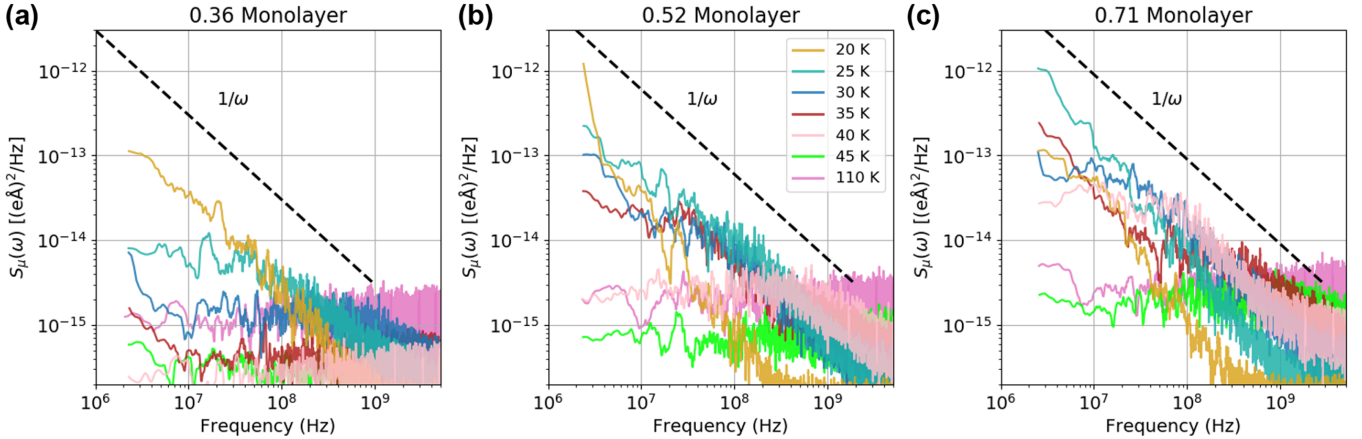


FIG. 4. $S_\mu(\omega)$ spectra obtained from dipole moment time-series data of the submonolayer coverage runs. The spectra were smoothed over a window of 12 time steps.

C. Submonolayer dynamics and spectra

Here, we examine the spectra produced by adsorbate dynamics at submonolayer coverages, as depicted in Fig. 4. The spectra notably contain regions that scale as $1/\omega$ between 10^6 and 10^9 Hz, which overlaps with the range of typical trap frequencies of 0.1–10 MHz.

The spectra can be divided into two general categories based on temperature. For moderate to high temperatures (>50 K), the noise is independent of frequency (white noise) and its magnitude increases with temperature. For low temperatures (20–40 K), the *high-frequency* noise is also flat and greater at higher temperatures, but the *low-frequency* noise behaves quite differently. At these temperatures, the noise levels increase with decreasing frequency with a mixture of $1/\omega$ and $1/\omega^2$ scalings before eventually flattening to a second white-noise region. Moreover, increasing the temperature leads to a decrease in the low-frequency noise ceiling and an increase in the cutoff frequency at which the ceiling is reached; this is similar to the behavior of TLF-derived systems, as discussed in Sec. II F.

Each of the different aspects of the low-temperature spectra can be matched to different types of movements. The high-frequency white noise stems from ubiquitous in-place adsorbate rattling of <2 Å, both in plane and out of plane, which causes random and uncorrelated dipole fluctuations. The low-frequency noise comes from movements, both individual and collective (see Fig. 5), that are sufficiently rare and substantial to give rise to different distinct dipole regimes between which the system fluctuates. Figure 19 illustrates this point by comparing the featureless spectrum of a particle with effectively no average dipole variation with the $1/\omega^2$ -containing spectrum of a particle that transitioned between two distinct dipole regimes.

At low temperatures, the source, and rarity, of the motions responsible for low-frequency noise can be traced back to the cohesive strength of the adsorbate clusters. As Fig. 6 shows, these clusters grow more cohesive with decreasing temperature and increasing N , and, at their strongest, are so cohesive that adsorbates routinely inhabit less-favorable surface facets in order to minimize their collective CH₄-CH₄ interactions. In these clusters, each adsorbate remains in a distinct location on the surface: although the adsorbates frequently rattle

in the x , y , and z directions, their average surface positions do not change. Crucially, this also means that their average dipole moments do not change (although the continual rattling makes their dipole values very noisy as a function of time). However, when perturbed enough, the clusters can undergo reconfigurations. This can be caused by individual particle motions, such as edge hopping, or, more often, correlated multiparticle motions, such as collective island shifts, internal ripples, and cluster rotations (Fig. 5). Either way, these reconfigurations change the global surface positions and, with them, the average dipole moments of one or more adsorbates; dipole changes can result from changes in the surface sites or z heights the different adsorbates occupy because of these motions. Such configuration-altering moves are rare at low temperatures since the CH₄-CH₄ attraction is high and the system's kinetic energy is low [lower than even some of the small surface barriers (see Table V)]. Because they are rare, these reconfigurations effectively divide the trajectories of each particle into distinct dipole fluctuation regions, each with different average dipole values.

This collection of dipole fluctuations among the system's particles aggregate to produce multiple average dipole states in the summed system dipole time-series data, an example of which can be seen in Fig. 7. These multilevel fluctuators give rise to $1/\omega$ features in the corresponding dipole-dipole fluctuation spectra in Fig. 4.

At higher temperatures, the CH₄-CH₄ interactions become smaller relative to each particle's kinetic energy. This leads to the clusters losing their cohesiveness (see Fig. 6) as particles more commonly move across the surface to new global positions. Instead of sampling different dipole regimes in different adsorbate cluster configurations (as in the low-temperature case), the particles now freely sample the whole surface with minimal hindrance [since the adsorbate surface barriers are not significant (see Table V)]. Unlike with the rare collective movements observed at low temperatures, this situation involves more common but substantially less correlated particle motions. As stated earlier, trajectories that randomly sample a single distribution produce white noise; thus, it is not surprising that these fluid surfaces give rise to featureless spectra. The magnitude of the high-temperature white noise increases with temperature because more of the higher-energy

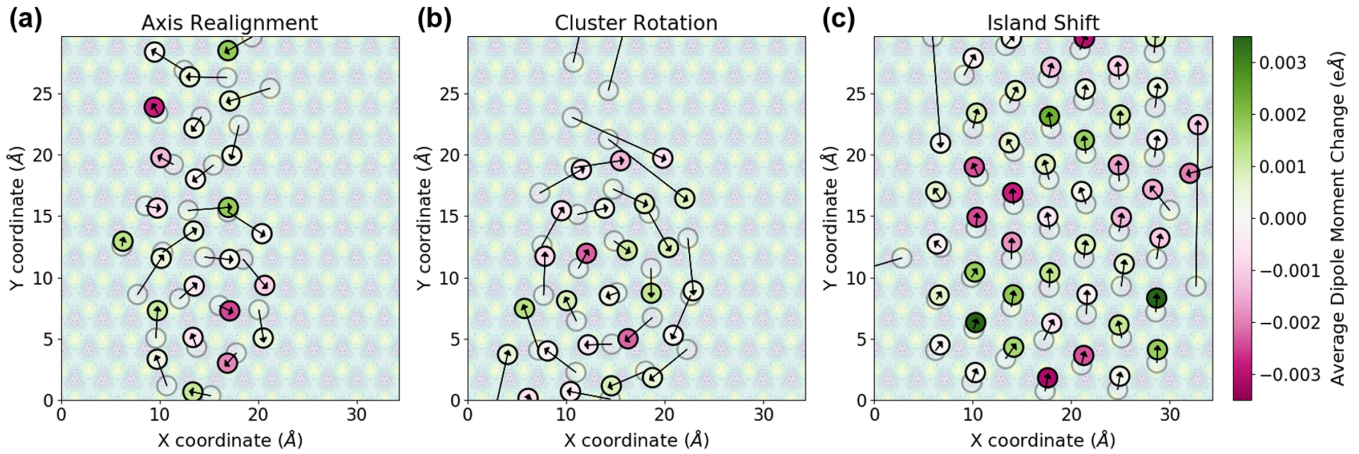


FIG. 5. Selected collective motions observed in submonolayer trajectories. Arrows point from each particle's initial position (represented by the dimmed circles) to its final position. The Au(111)-induced dipole surface [from Fig. 1(b)] is faintly shown beneath the particles. The axis realignment (a), in which the particles reorient around a new axis, and cluster rotation (b) examples are taken from the 0.36-ML trajectory at 20 K, while the island shift (c) example is from the 0.71-ML trajectory at 30 K. Such motions can take on the order of 10's or the low 100's of ps to occur.

z positions (and thus larger dipoles) are accessed by the particles at higher temperatures. Table III summarizes the trends discussed for the low-temperature and high-temperature submonolayer spectra.

Identifying correlated motions is not always straightforward, as they come in many varieties (as can be seen in Fig. 5). We used a number of methods to identify relevant motions. Tracking the number of neighbors each particle can identify particles migrating around or approaching cluster edges. Examining how cluster axial angles vary can identify cluster rotations. However, the most reliable way of identifying meaningful movements was to parse dipole moment time-series data and look for substantial changes in the average dipole moment, such as that shown in Fig. 19. The averaging step is critical, as the dipole data are very noisy from time step to time step.

It is important to emphasize that the frequency of the movements discussed may vary from run to run. Because these events are rare, sampling sizes and stochasticity will invariably play a role in how often they happen in a (relatively short) simulation, and such effects will be felt more greatly at lower temperatures. These effects will in turn influence the corresponding feature frequencies and magnitudes in the dipole-dipole fluctuation spectra. Nevertheless, these results illustrate how a series of collective motions that are sufficiently rare (due to temperature, cluster cohesion, and weak-but-existent surface barriers) can produce $1/\omega$ scaling at low frequencies on a model trap surface.

D. Supermonolayer dynamics and spectra

We next examine the spectra produced by adsorbate dynamics at monolayer and supermonolayer coverages. Despite having more adsorbates than the submonolayer coverages, the monolayer trajectories produce featureless spectra. Although there are more adsorbate-adsorbate interactions, there is not enough room for significant surface movements with the surface fully covered. As with the submonolayer coverages, some particles reside in higher-energy atop sites due to the competition between the surface-adsorbate and OPLS interactions, but unlike the submonolayer adsorbates, the monolayer adsorbates do not move significantly and thus cannot significantly contribute to the noise or dipole-dipole fluctuation spectra.

The spectra produced by supermonolayer dynamics, on the other hand, show several sets of features, as seen in Fig. 8. At low temperatures (<60 K), spectra display scalings of ω^{-1} mixed with some ω^{-2} until around 35 K, when the spectra become nearly flat (see also Fig. 24). At higher temperatures (>70 K), however, a new set of larger-magnitude TLF-like features supersede the low-temperature features. These features increase in noise magnitude until roughly 90–110 K (depending on the coverage) before declining with a corresponding increase in cutoff frequency. These high-temperature supermonolayer features cover a greater range of noise magnitudes and frequencies than any of the other spectral features we found.

1. Low-temperature supermonolayer dynamics

At low temperatures, adsorbates on filled supermonolayer surfaces are mainly static (apart from in-place rattling), but they can be affected by second-layer adsorbates in ways that lead to individual and collective first-layer motions (see Fig. 9). Even a stationary second layer affects first-layer particles: adsorbates with more neighboring second-layer particles [at most three, as can be seen in Fig. 2(b)] are pushed down to lower surface heights than those with no such neighbors (see Fig. 10). But, second-layer particles can and do migrate

TABLE III. Summary of submonolayer results.

Temp.	Clusters	Surf. Moves	Corr.	$1/\omega$	$1/\omega^2$
20–40 K	Strong	Rare	High	10^6 – 10^9 Hz	10^6 – 10^8 Hz
>50 K	Weak	Common	Low	Not seen	Not seen

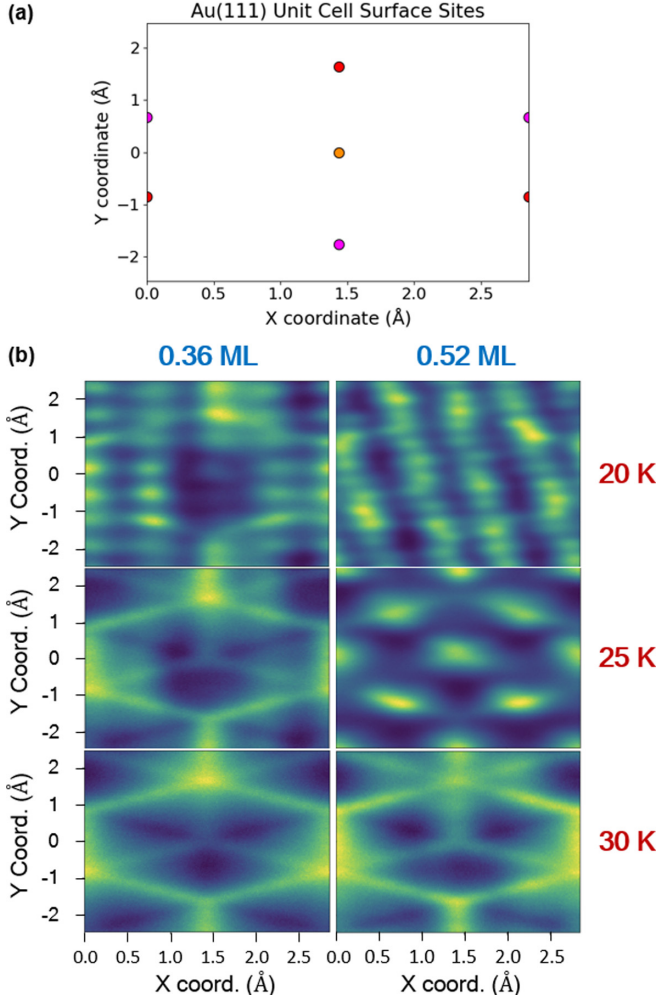


FIG. 6. Two-dimensional normalized histograms of the relative positions of CH_4 adsorbates on the Au(111) unit-cell surface for selected submonolayer coverages. (a) Surface facets for reference (see Fig. 1). (b) Unit-cell adsorbate position histograms. At lower temperatures, a larger proportion of the particles reside near less favorable atop and bridged sites due to the strength of the adsorbate clustering. As the temperature increases, the adsorbate clusters become more fluid, and individual particles are able to migrate along the surface more often and end up residing in more favorable sites.

around the unfilled second layer to different global positions. Similar to the submonolayer case, such movements happen more often with increasing temperature, but second-layer particles are even more weakly held by the surface potential than surface particles despite experiencing OPLS interactions from first-layer particles (see and thus migrate more frequently at lower temperatures). As these second-layer particles migrate, at rare intervals on the ps timescale but plenty of times over the course of a μs -scale trajectory, they end up influencing different sets of first-layer particles at different points in the trajectory, thus giving rise to different average surface height (and, with them, average dipole) regimes for those surface particles at those times (see Fig. 9). When enough particles experience these second-layer-induced changes, the total system dipole is moved into a different regime as well, leading to features in the dipole-dipole fluctuation spectra.

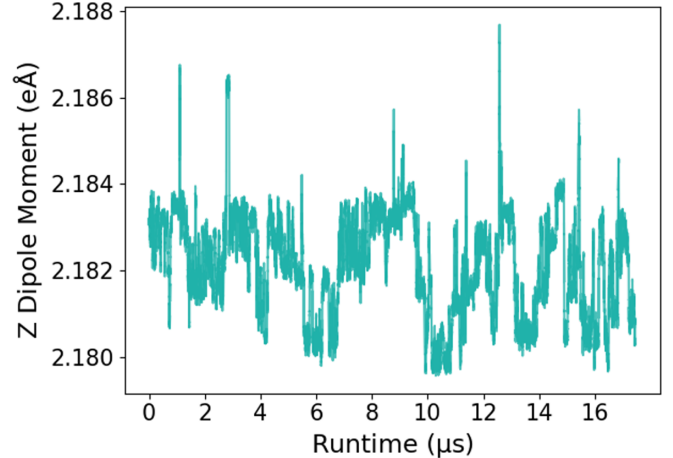


FIG. 7. 10 000-frame moving average of the summed system dipole from a 0.71-ML coverage trajectory run at 25 K. Multiple average dipole states emerge across the course of the simulation. This set of fluctuations gives rise to $1/\omega$ features in the corresponding $S_\mu(\omega)$ spectra.

Supermonolayer surfaces can also undergo collective motions as a result of second-layer particle migrations that perturb the surface in the right way, as can be seen in the examples in Fig. 9. However, these motions only seem to consist of slight cluster shifts and ripples rather than the diversity of submonolayer collective motions highlighted by Fig. 5; this is likely due to submonolayer surfaces having far more room to maneuver than filled-up supermonolayer surfaces.

Although second-layer particles are responsible for first-layer dipole regime changes, their own dipole changes are minimal and do not contribute to overall noise levels. Figure 11 shows why this is: At typical second-layer distances from the surface, adsorbate dipole moments are nearly zero and have virtually no variation. Although this makes movement within the second layer noiseless, it makes movement between layers significant in dipole terms, as the next section will detail.

2. High-temperature supermonolayer dynamics

Starting at intermediate temperatures (between 70 and 90 K), the supermonolayer spectra diverge more decisively from the submonolayer spectra. Whereas submonolayer spectra do not contain lower-frequency noise features at higher temperatures, supermonolayer spectra demonstrate large low-frequency shoulders orders of magnitudes larger than any of the submonolayer low-frequency features. The emergence of

TABLE IV. Summary of motions and the corresponding range of average per-particle dipole moment magnitude changes that they cause.

Motions	Coverages	Avg. dipole changes
Collective surface motions	<1 ML	<5 me Å
Layer-2 pushing	>1 ML	3–10 me Å
Surface shifts	>1 ML	<3 me Å
Layer exchanges	>1 ML	38–48 me Å

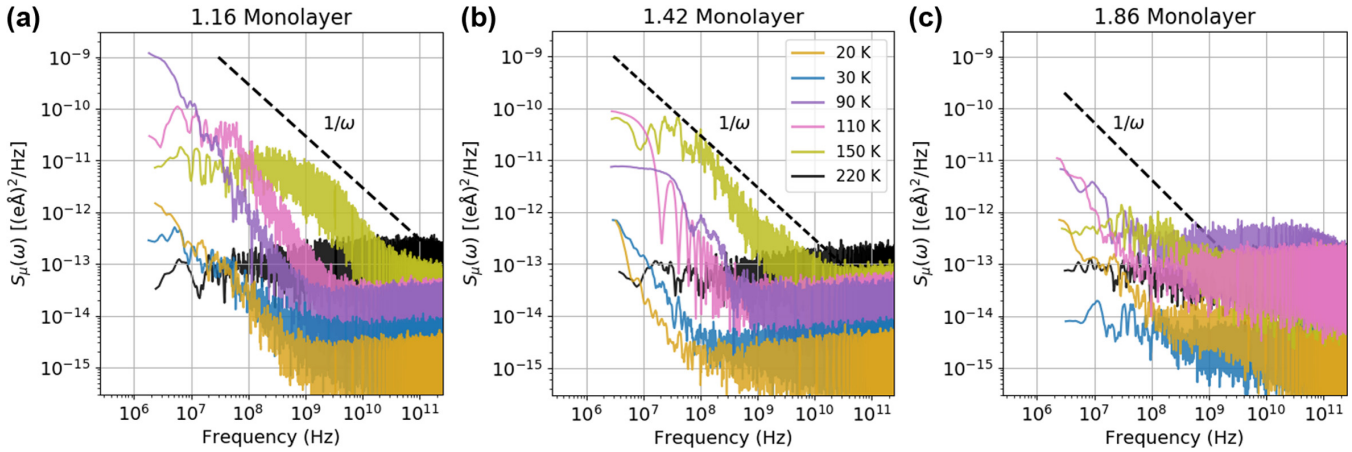


FIG. 8. $S_\mu(\omega)$ spectra obtained from three different supermonolayer coverages over a range of temperatures. The spectra were smoothed over a window of five time steps.

such shoulders indicates that there is an additional, larger noise source present at high temperatures that is absent at lower coverages. It turns out that this noise stems from movements of adsorbates *between* layers, which we refer to as layer exchanges. Unlike the submonolayer motions in Fig. 5, layer exchanges occur in the span of a few ps, and they have a larger impact on particle and system dipoles (see Table IV).

Figure 12 demonstrates how layer exchanges translate into the larger spectral noise observed. Of the three particles depicted, only the one that exchanged layers produces any low-frequency features. Figure 11 shows why layer exchanges produce more noise than any surface-adsorbate motions. When a particle transitions from the first to the second layer, its dipole moment drops from roughly 0.044 to nearly 0 e \AA , which is a drop several orders of magnitude larger than any fluctuation in the dipole moment due to first-layer sur-

face motions alone (and compared to the motions shown in Fig. 5).

With large dipole changes and long mean state residence times, layer exchanges can produce significant low-frequency TLF noise in the spectra of individual particles [per Eq. (11)]. However, the spectra produced by the system's total dipole moment will only be affected if layer exchanges change the makeup of the surface, where the most significant induced dipole moments are possible (see Fig. 11). Therefore, only *unidirectional* layer exchanges, rather than a set of reciprocal exchanges, will contribute to the spectra seen in Fig. 8.

As noted in Sec. III A, our simulation cell can support 68- and 70-adsorbate surfaces in addition to the previously defined monolayer surface of 69 adsorbates. Second-layer OPLS interactions can make less-favorable monolayer surface populations more accessible as well. Unidirectional layer

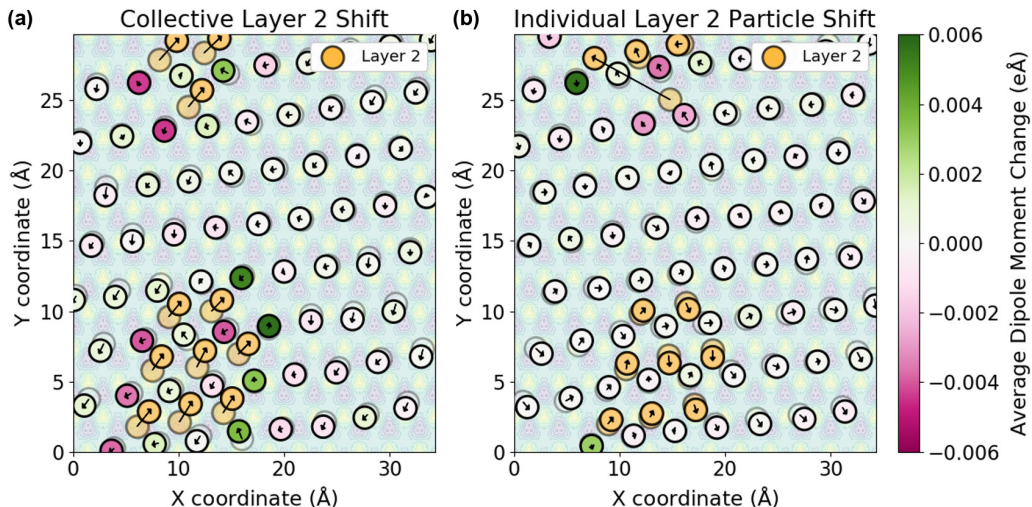


FIG. 9. Depiction of (a) collective and (b) individual second-layer particle movements and their effect on the average dipoles of surface adsorbates. Both examples are taken from segments of the 1.16-ML trajectory at 20 K. Arrows point from each particle's initial position (represented by the dimmed circles) to its final position. Here, only first-layer particles are colored with the color map; second-layer particles, which exhibit virtually no dipole variation (see Fig. 11), are colored yellow (medium gray). As second-layer particles move, they significantly impact nearby first-layer particles, especially those that gain or lose second-layer neighbors. In this way, the movement of particles in the unfilled second layer can cause surface dipole changes and position shifts.

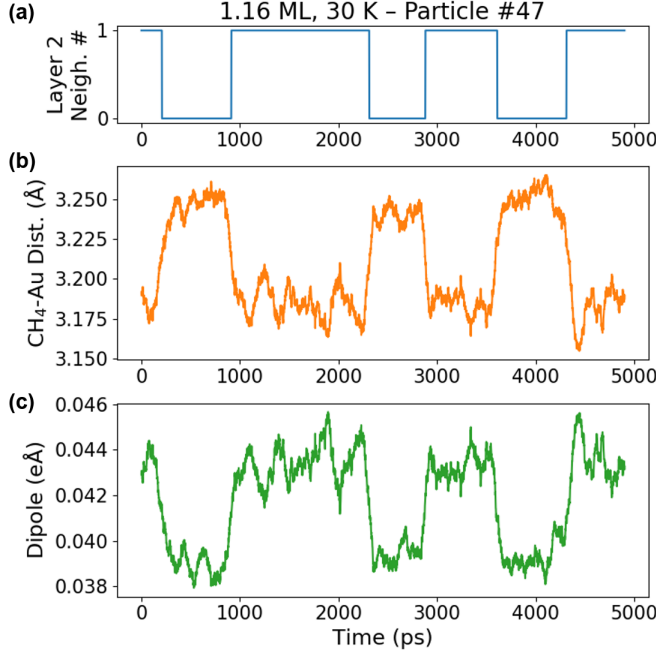


FIG. 10. An example of the effect of second-layer neighbors on surface adsorbates, taken from a segment of the 1.16-ML trajectory at 30 K. (a) Number of second-layer particles neighboring particle No. 47. (b) 100-frame rolling average of particle No. 47's distance from the surface. (c) 100-frame rolling average of particle No. 47's dipole moment. When a second-layer particle migrates to particle No. 47's neighborhood, it pushes the particle to a distinctly different average dipole regime.

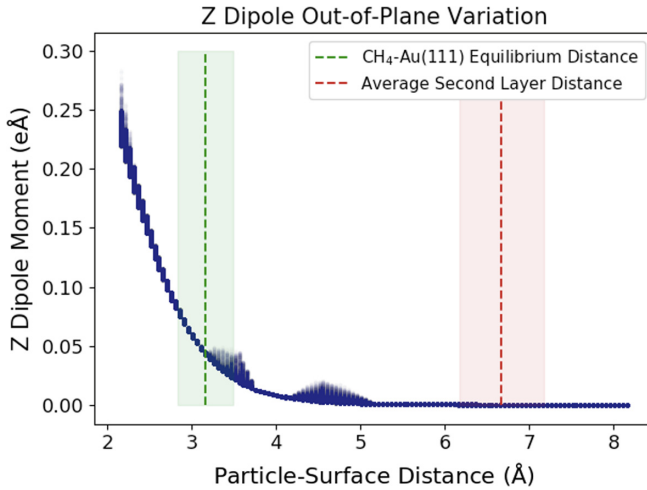


FIG. 11. Plot of all possible particle z dipole moments (across all x and y surface positions) versus the particle's distance from the electrode surface. The dark blue shading indicates how often the (dipole, distance) pair is generated from the interpolation script at different (x, y) values for that distance; the bumps around 3–3.75 and 4–5 Å are from dipole sensitivity to (x, y) changes at those distances. The two layers are marked with mean surface distances (dotted lines) and 95% confidence intervals (shaded regions) calculated from supermonolayer particles at 60 K. The first layer experiences a range of dipole moment changes from small shifts in any direction. Although the second layer contains virtually no dipole variation, the change in dipole moment from going between layers is an order of magnitude greater than any dipole changes within the first layer.

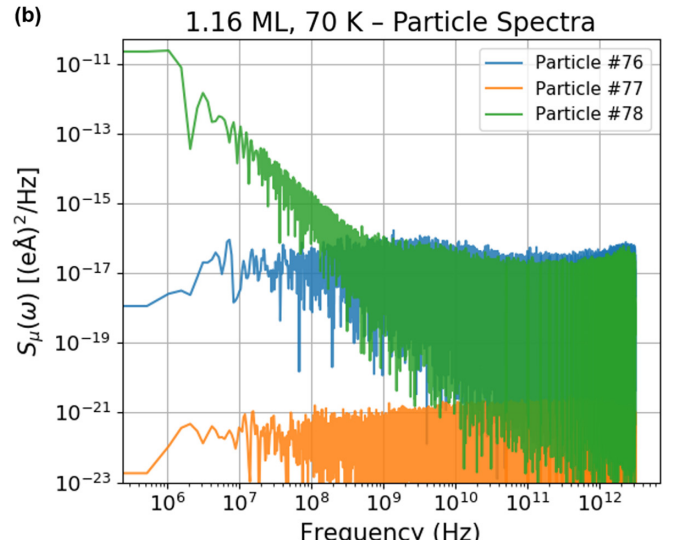
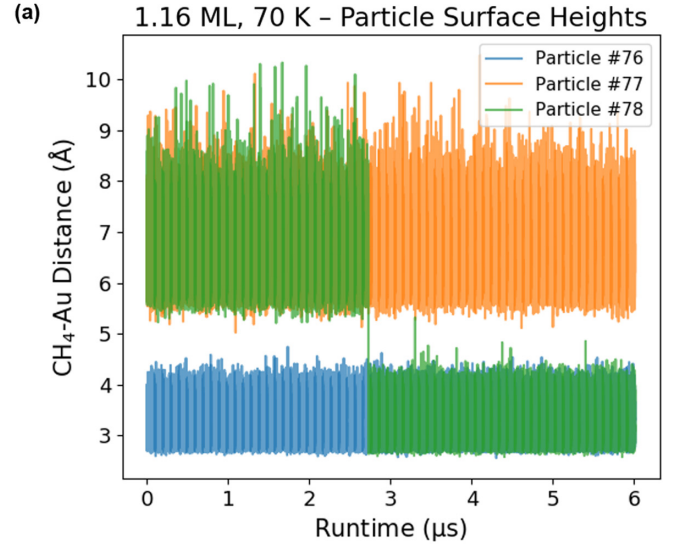


FIG. 12. (a) Surface-adsorbate distances of selected adsorbates taken from the 1.16-ML trajectory at 70 K. Adsorbate No. 78 undergoes a layer exchange that alters its surface-adsorbate distance around 2.75 μ s, while adsorbates Nos. 76 and 77 remain in their original layers. (b) Corresponding single-particle dipole-dipole fluctuation spectra of the selected adsorbates.

exchanges act to transition the system between these different surface populations. An example of this in the 1.16-ML coverage is shown in Fig. 13. It is this effect of losing or gaining a particle (and its large induced dipole) from the surface that leads to the system state fluctuation that produces features in the spectra in Fig. 8.

As with the submonolayer surface movements, the frequency of layer exchanges may vary from run to run. With mean residence times in the microseconds for some runs, the spectra can be sensitive to additional exchange events or a change in the time that they occur. For this reason, these results are not meant to precisely recreate experimentally observed spectra. Nevertheless, these results illustrate how thermally activated layer exchanges can give rise to $1/\omega$ scaling regions at low frequencies on a model trap surface.

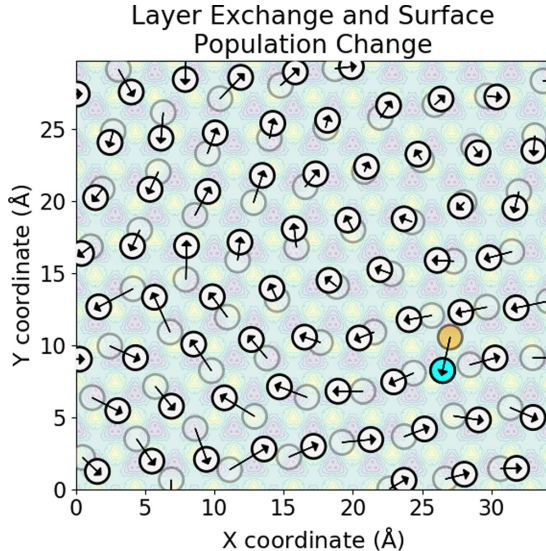


FIG. 13. Layer exchange that results in a surface population change, taken from a 1.16-ML trajectory segment at 70 K. The yellow (gray) circle denotes the second-layer particle before exchanging layers, while the blue (dark gray) circle shows the same particle after descending to the first layer.

3. Layer exchanges as two-state thermally activated fluctuations

One can consider layer exchanges as a two-state activated process of the kind discussed in Sec. II F. Adsorbates can either inhabit layer 1 (nonzero dipole moment) or layer 2 (near-zero dipole moment) and can stochastically change layers abruptly. The layer exchanges in our simulations do not perfectly adhere to this paradigm, as layer 1 particles exhibit a range of values with a variance of around 4.5×10^{-3} eÅ rather than one single value. However, the layer-2 particles can be represented by a state with a dipole value of zero with little loss of precision (see Fig. 11). The typical layer-(1 → 2) dipole difference of 4.4×10^{-2} eÅ is an order of magnitude larger than the layer-1 dipole variance, ensuring that the magnitudes of layer-(1 ↔ 2) transitions are outside the distribution of layer-1 dipole values. Although layer exchanges are individual motions, this treatment can be extended to the total system dipole moment, where states can be defined by layer populations each differing by roughly 4.4×10^{-2} eÅ.

To see how well this random telegraph signals (RTS) model describes our simulated spectra, we calculated analytical spectra from Eq. (11) based on parameters from the corresponding simulations. ΔI was set to 4.4×10^{-2} eÅ to represent the magnitude of the typical dipole fluctuation from one adsorbate vacating or joining the surface. To estimate τ_0 and τ_1 , we calculated the average residence times of each surface population that the system experienced. For simplicity, here we present analysis performed on transitions between two layer populations. In our trajectories, typical τ_0 and τ_1 values ranged from the 100's and 1000's of ns at 90–110 K to the 10's of ns at 150 K.

Figure 14 compares TLF analytical spectra calculated from Eq. (11) with spectra obtained from selected 1.42-ML trajectories. In addition, Fig. 18 repeats this comparison using per-particle spectra. Although the simulated spectra are noisier,

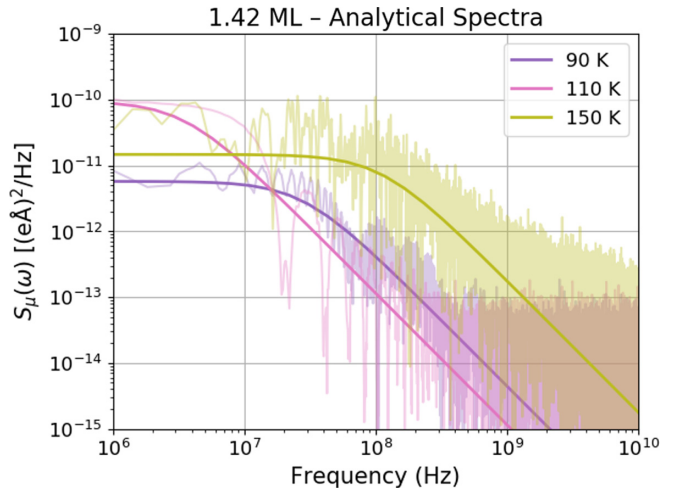


FIG. 14. Comparison of simulation spectra (lighter shade) and analytical spectra calculated from the two-level fluctuator model (darker shade) for selected 1.42-ML trajectories.

they follow the same frequency and magnitude trends as the analytical spectra. In particular, the relative separation between the different trajectories and the ordering of the low-frequency leveling off is captured by the analytical spectra.

Figure 14 and Eq. (11) provide a rationale for why the low-frequency magnitudes of the supermonolayer spectra increase with decreasing temperature. Increasing system temperature results in more frequent layer exchanges; in RTS terms, this can be seen as decreasing *both* τ_0 and τ_1 since the more often layer exchanges occur, the less time a particle spends in a given layer. In the low-frequency limit of Eq. (11), the noise magnitude is inversely proportional to the $[(1/\tau_0) + (1/\tau_1)]^2$ term, which means that shorter residence times will decrease the magnitude of the noise. This behavior is similar to that displayed in Fig. 17.

The addition of the high-frequency white noise and two-state fluctuator regions of the spectra gives us the spectral form we see in our supermonolayer coverages above 70 K.

IV. CONCLUSIONS

In this work, we have analyzed the dynamics of methane adsorbates on gold electrodes (as a realistic, but model system) based upon first-principles potentials with the aim of identifying the adsorbate motions that give rise to anomalous heating in ion traps. Based upon an extensive set of molecular dynamics simulations run at a wide range of temperatures and surface coverages, we were able to correlate adsorbate motions such as cluster reconfigurations and layer exchanges with different frequency-dependent features of the adsorbate dipole-dipole fluctuation spectra that ultimately relate to electric-field noise in the trap. Counter to prevailing intuition, we find that accounting for adsorbate-adsorbate correlations is pivotal for observing $1/\omega$ frequency scaling and that rare, fundamentally collective adsorbate motions are responsible for the $1/\omega$ features in these spectra at MHz frequencies. In contrast, single (noninteracting) adsorbate vibrational motions or surface diffusion lead to white noise up to frequencies orders of magnitude larger than those observed

in ion traps. In particular, we find that the collective rotations or translations of strongly interacting adsorbates within clusters give rise to $1/\omega$ scaling at submonolayer coverages, while layer exchanges of adsorbates between the first two adsorbate monolayers are the greatest source of $1/\omega$ scaling at supermonolayer coverages. Key features of our simulated spectra can be reproduced by an ensemble of two-level fluctuator models parametrized with the intensities and residence times associated with these motions, strongly corroborating our findings. This work thus establishes that rare (rather than intrinsically low-frequency) motions of adsorbates (accessible with molecular dynamics simulations of realistic systems) can be understood as one source of anomalous heating that is consistent with experimental observations, dispelling the notion that adsorbate motions are too high in frequency to be key contributors.

That said, our model involved a number of notable simplifications. First, our methane adsorbates were treated as classical point masses, which enabled us to treat the methane-methane interactions via an OPLS potential rather than in a fully *ab initio* manner. While this is a reasonable simplification for a spherically symmetric molecule like methane, extensions of this approximation would be needed for larger hydrocarbons containing many more intramolecular vibrational and rotational degrees of freedom. Second, we did not take any nuclear quantum effects into account. These could become important at the lowest temperatures explored here and would open up the possibility of the methane adsorbates more readily traversing the gold surface. While tunneling would not impact the $1/\omega$ scaling that emerges due to layer exchanges above 70 K, it could affect the forms of the submonolayer spectra, an issue which would have to be investigated in future studies. Moreover, our single-crystalline gold electrodes were atomically smooth; while in practice most electrodes consist of polycrystalline materials or possess a wide range of defects, the approximation of local smoothness on the scale we have studied is reasonable. However, for a more realistic model at larger length scales (and potentially including additional interaction effects), additional surface structures would need proper accounting: it is likely that adsorbates traversing such uneven surfaces would generate additional (rare) dipole fluctuations and, consequently, low-frequency electric-field noise. Even different smooth surfaces can have noticeable variation in surface dipole profiles, as recent theoretical work on carbon adsorbed on gold demonstrated [57]. Lastly, throughout this work, we have relied upon the patch potential model to link dipole fluctuations to trap noise even though it is only one approximate model of many potential models for this noise [32]. For these reasons, our model is not meant to precisely reproduce experimental spectra, but rather to provide insights regarding the microscopic origins of anomalous heating associated with fluctuating induced dipoles on adsorbed molecules, which we suggest does generalize to even more realistic models and systems. In addition, the specific choice of methane on gold as a model system presents the relevant spectral features of interest, but it also readily extends to other combinations of adsorbates and surface materials for direct comparison with specific experimental circumstances by modifying the interaction parameters either empirically or by using *ab initio* calculations to determine the parameters.

Despite these simplifications, our model still reveals a variety of regions with $1/\omega$ scaling. The fact that it did so without involving multiple types of adsorbates or accounting for intramolecular vibrational degrees of freedom suggests that the mere presence of even simple molecules on electrode surfaces can lead to anomalous heating consistent with experiments. This points to a universal molecular origin for this phenomenon. Even so, more massive hydrocarbons involved in the trap fabrication process or associated with ambient contamination, such as isopropanol, photoresist fragments, or polymerized carbon species, are much more likely than methane to be adsorbed onto electrode surfaces. These more massive hydrocarbons would be expected to interact more strongly with the surface and to exhibit larger, more varied dipole moments, most likely shifting the $1/\omega$ scaling regimes we observed to even lower frequencies. More strongly interacting hydrocarbons would also be expected to shift the observed $1/\omega$ spectra to the higher temperatures employed in many experiments. Molecules with more vibrational degrees of freedom are additionally more likely to give rise to motions that can be activated in different frequency regimes, which would result in the emergence of multiple, overlapping two-level or multilevel fluctuators that can combine to yield $1/\omega$ scaling over a much larger frequency range [43]. We thus look forward to future simulations of the noise produced by a variety of interacting adsorbates with many degrees of freedom, which may hold the key to reproducing experimental spectra with even greater fidelity.

The data that support this study, including the DFT adsorption energies and dipole moments used to compute dipole-dipole autocorrelation functions and fluctuation spectra, are available online [53].

ACKNOWLEDGMENTS

The authors thank D. Hite, J. Sage, J. Sedlacek, J. Chiarerini, and H. Häffner for helpful discussions. This work was performed under the auspices of the U.S. Department of Energy by Lawrence Livermore National Laboratory under Contract No. DE-AC52-07NA27344. We also thank the Brown Presidential Fellowship Program for financially supporting Y. Liu. Part of this research was conducted using computational resources and services at the Center for Computation and Visualization, Brown University.

APPENDIX A: METHANE-GOLD POTENTIAL ENERGY SURFACE

Table V below contains the barrier heights between every pair of different sites on the PES at the minimum energy adsorbate-surface height (as depicted in Fig. 1).

TABLE V. Surface potential barrier heights.

Barrier type	Barrier height (K)	Barrier height (eV)
Atop-bridged	0.35	3×10^{-5}
Atop-hollow	1.16	1×10^{-4}
Bridged-hollow	1.97	1.7×10^{-4}
Hollow-bridged	24.37	2.1×10^{-3}
Bridged-atop	35.16	3×10^{-3}
Hollow-atop	58.37	5×10^{-3}

TABLE VI. Run times of the spectra featured in this work.

Coverage (N_{CH_4})	Run time (μs)
0.36 ML (25)	19
0.52 ML (36)	17
0.71 ML (49)	17
1.0 ML (69)	4
1.16 ML (80)	9–12
1.42 ML (98)	6–7
1.86 ML (128)	6–9

APPENDIX B: ADDITIONAL SIMULATION INFORMATION

Table VI contains the run times of the spectra featured in Sec. III.

APPENDIX C: EQUILIBRIUM SURFACE COVERAGES

To arrive at our equilibrium monolayer surface coverage of 69 particles, we searched for the monolayer coverage with the lowest energy and visually inspected the related configurations to ensure they were homogeneous. Figure 15 shows how interparticle and surface energies vary with the number of adsorbates. Any attempts to add more particles beyond 74 resulted in particles getting ejected from the surface. Although there is another local per-particle energy minimum at $N = 66$, the ability to add more surface particles (and thus lower overall system energy) pushes the size of the monolayer to 69 particles. OPLS energies of the cluster particles are the major factor in determining the favorability of surface coverages. Both 68- and 70-adsorbate coverages are at low enough energies that supermonolayer coverages can transition between these states and the 69-adsorbate monolayer when the temperature is high enough for layer exchanges to occur.

Figure 16(a) depicts the largest submonolayer coverage ($N = 49$) featured in this work, and Figs. 16(b) and 16(c) depict two representative supermonolayer coverages. As the loosely held second layer grows in size, it becomes more difficult to maintain its cohesion in the simulations. Higher temperatures can increase this difficulty. This can lead to second-layer particles being pushed to or drifting to surface heights beyond the second layer. We noticed that this can happen in the $N = 128$ runs to a few particles as temperatures are increased. This can have the effect of reducing the effective coverage from 1.86 ML to between 1.77 and 1.84 ML, depending on the number of particles. However, because the dipole variation is virtually nonexistent by second-layer distances, these few particles do not see their dipoles affected by this behavior.

APPENDIX D: TWO-LEVEL FLUCTUATORS AS A SOURCE OF $1/\omega^2$ AND $1/\omega$ NOISE

As discussed in the body of the paper, our electric-field fluctuation spectra exhibit several key frequency scalings. Many of these scalings have well-known connections to certain types of fluctuations in the signal processing literature

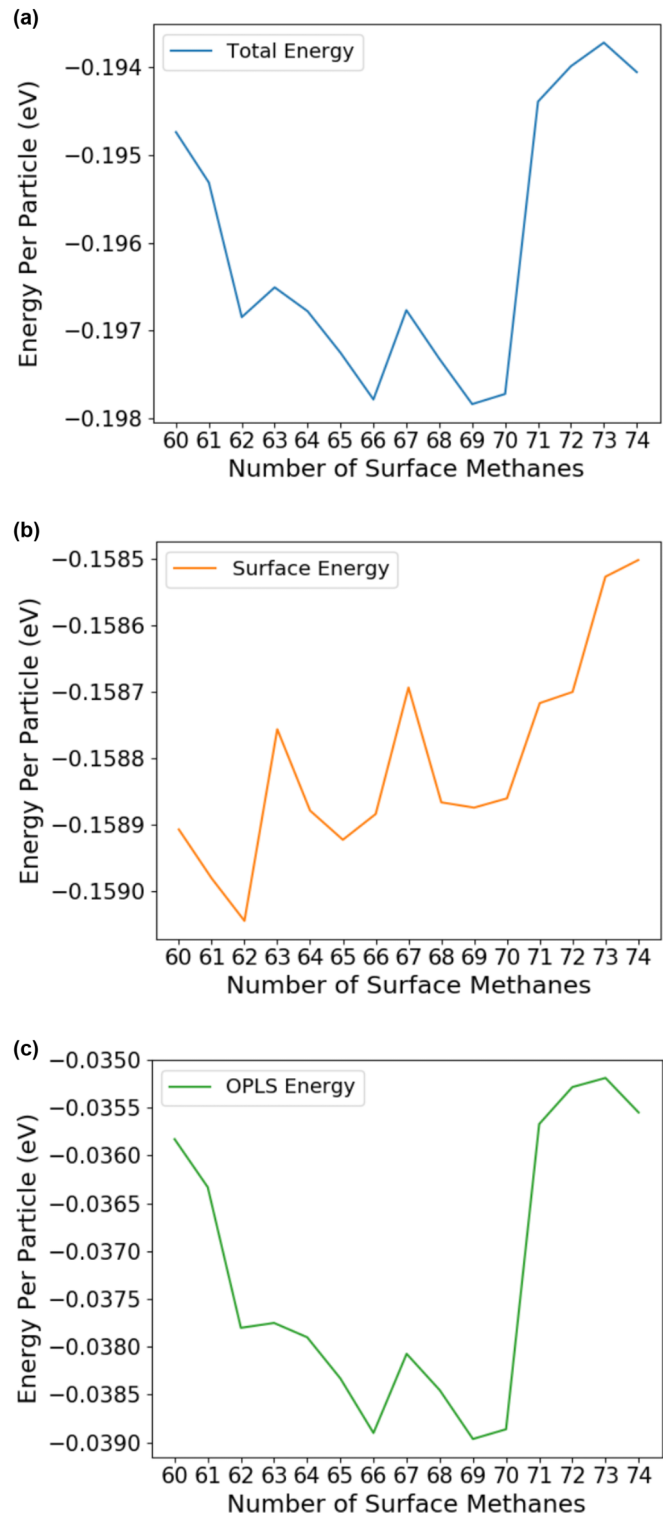


FIG. 15. Energy contributions to the energy per particle as a function of the number of methanes on the surface. The OPLS energy (c) is the main factor in determining the per-particle energy of monolayer coverages [note that the range of variation in the entire surface energy plot (b) is on the scale of the variation between two neighboring tick marks in the OPLS energy plot]. This reflects the strength of the OPLS potential relative to x, y methane-gold barriers at the surface.

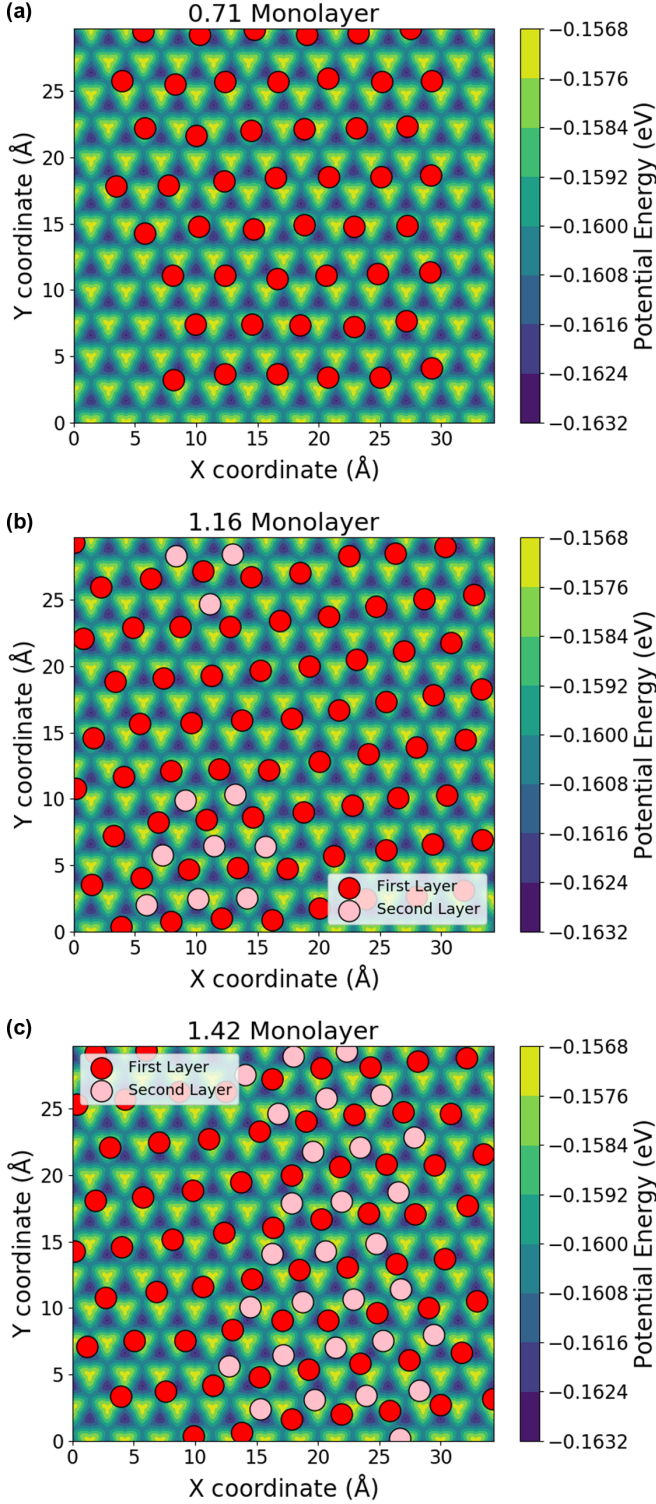


FIG. 16. Representative snapshots of (a) 49 adsorbates (0.71 ML coverage); (b) 80 adsorbates (1.16 ML coverage); (c) 98 adsorbates (1.42 ML coverage). The red (dark gray) and pink (light gray) circles denote the particles in the first and second layers, respectively. These illustrate the nearly regular pattern that emerges among particles at sufficiently high densities, even though this pattern is incommensurate with the underlying surface potential. At sufficiently high second-monolayer coverages, patterns emerge in second-layer particle configurations.

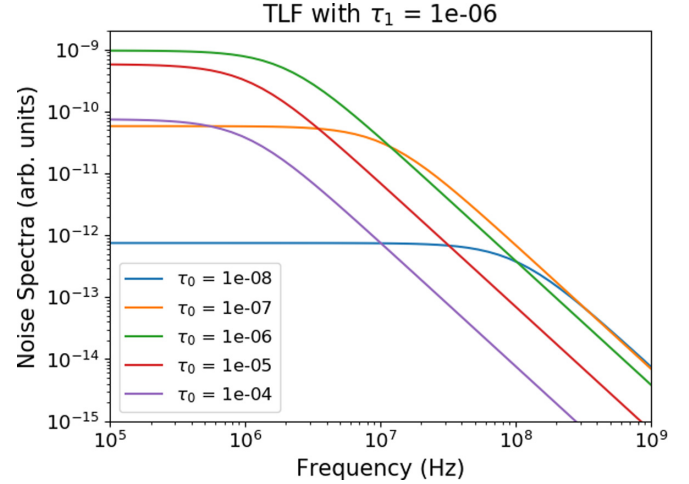


FIG. 17. Examples of TLF noise spectra with τ_1 fixed at $10\ \mu\text{s}$ and τ_0 varied (similar to Fig. 4.6 in Zanolla [43]). ΔI was set to 0.044, the same magnitude as the layer-(1 \leftrightarrow 2) transitions. TLF noise reaches a maximum when $\tau_0 = \tau_1$. When $\tau_0 > \tau_1$, TLF noise decreases while the cutoff frequency [$\omega_c = (1/\tau_0 + 1/\tau_1)$] remains mostly unchanged. When $\tau_0 < \tau_1$, TLF noise decreases and ω_c increases, effectively shifting the frequency curve to the right.

that also arise in our simulations. For instance, a quantity that fluctuates randomly about a single average value with no correlation in time leads to featureless (white) noise [58] in the frequency domain. On the other hand, a quantity that transitions between two distinct values produces a region of $1/\omega^2$ frequency scaling; systems that fluctuate like this are known as two-level fluctuators [42] (TLFs) or random telegraph signals (RTS) [43]. A quantity that switches between states 0 and 1, differs in value by ΔI , and has mean state residence times of τ_0 and τ_1 will yield spectra of the following form [56]:

$$S(\omega) = \frac{4(\Delta I)^2}{(\tau_0 + \tau_1)[(1/\tau_0 + 1/\tau_1)^2 + \omega^2]}. \quad (\text{B1})$$

When $\tau_0 = \tau_1 = \tau$, this expression simplifies to

$$S(\omega) = \frac{4(\Delta I)^2 \tau}{1 + \tau^2 \omega^2}. \quad (\text{B2})$$

Equations (B1) and (B2) produce white noise at low frequencies followed by a rounding off to a $1/\omega^2$ descent at frequencies greater than a cutoff frequency, given by $\omega_c = (1/\tau_0 + 1/\tau_1)$. Figure 17 shows how TLF noise varies with τ_0 at constant τ_1 . Here, TLF noise reaches a maximum when $\tau_0 = \tau_1$. When $\tau_0 > \tau_1$, TLF noise decreases while ω_c remains mostly unchanged; when $\tau_0 < \tau_1$, TLF noise decreases and ω_c increases, effectively shifting the frequency curve to the right [43]. In general, decreasing τ_0 and τ_1 will shift the $1/\omega^2$ region to higher frequencies.

In addition to $1/\omega^2$ scaling, TLFs can give rise to $1/\omega$ regions in several ways. Every individual TLF has sections of $1/\omega$ and near- $1/\omega$ scaling in the rounding-off region between the white-noise and $1/\omega^2$ regimes. Moreover, an ensemble of TLFs with different transition frequencies can produce an aggregate $1/\omega$ region over several decades of frequencies

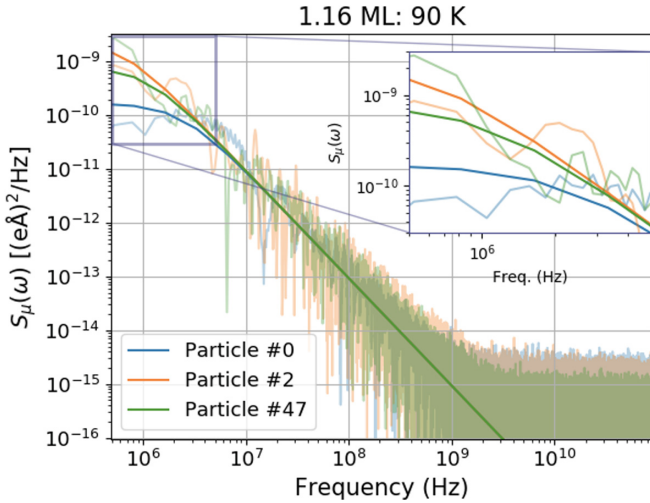


FIG. 18. Comparison of simulated spectra (lighter shade) and analytical spectra calculated from the two-level fluctuator model (darker shade) for selected particles of the 1.16-ML run at 90 K.

[43]; fluctuators with more than two levels can also combine together to produce $1/\omega$ regions in a similar manner.

APPENDIX E: PLOTS OF TLF SYSTEM BEHAVIOR

Figure 18 shows the results of fitting per-particle spectra (of the 1.16-ML coverage at 90 K) with the TLF model

using mean layer residence times. Figure 14 uses a similar approach with the full spectra (with the 1.42-ML coverage at selected temperatures). Figure 19 compares 0.71-ML per-particle spectra segments of a particle with one average dipole regime and another with two average dipole regimes. Only the particle with two regimes shows a region of the TLF scaling of $1/\omega^2$.

APPENDIX F: TIME-CORRELATION FUNCTIONS THAT UNDERLIE DIPOLE-DIPOLE FLUCTUATION SPECTRA

One challenge associated with computing trap noise spectra based upon dipole-dipole correlation functions is deciding what form the correlation functions should assume. Given that our dipole data are two dimensional ($\mathcal{T} \times N$), we have two broad options. If we decided we wanted to compute the autocorrelation function of the *summed* total dipole moment of all adsorbates, we would use the following expression:

$$C_{\mu,\mu}(\tau) = \frac{1}{(\mathcal{T} - \tau)} \sum_{k=1}^{\mathcal{T}-\tau} \left[\left(\sum_i^N [\mu_{i,z}(t_k)] - \langle \mu_z \rangle \right) \times \left(\sum_j^N [\mu_{j,z}(\tau + t_k)] - \langle \mu_z \rangle \right) \right]. \quad (\text{D1})$$

If we instead wanted to first compute the dipole autocorrelation functions of each *individual* particle and then sum them

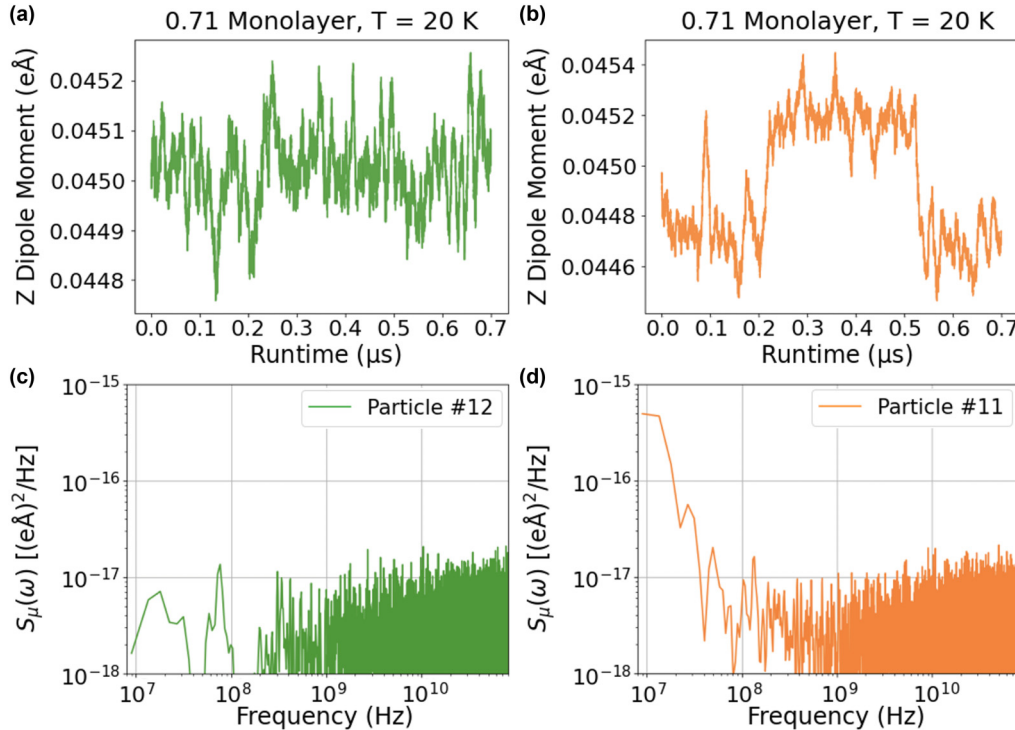


FIG. 19. Emergence of low-frequency $S_\mu(\omega)$ noise in a 0.7-μs stretch of the 0.71-ML run at 20 K. The top panels show the 10 000-frame moving average of the z dipole moment for two different adsorbates: (a) particle No. 12, which shows deviations from a single value of 4.5×10^{-2} eÅ, and (b) particle No. 11, which shows two distinct dipole regions separated by 5×10^{-4} eÅ. The bottom panels show the corresponding FT spectra for each particle: (c) because particle No. 12 never fluctuates between discrete average dipole regions, its spectrum is featureless; (d) because particle No. 11 fluctuates between two dipole regions, its spectrum has the TLF scaling of $1/\omega^2$.

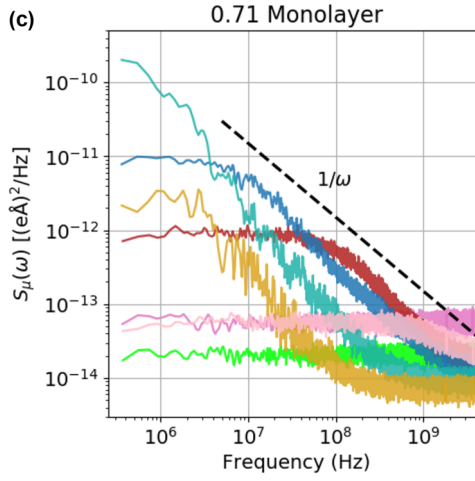
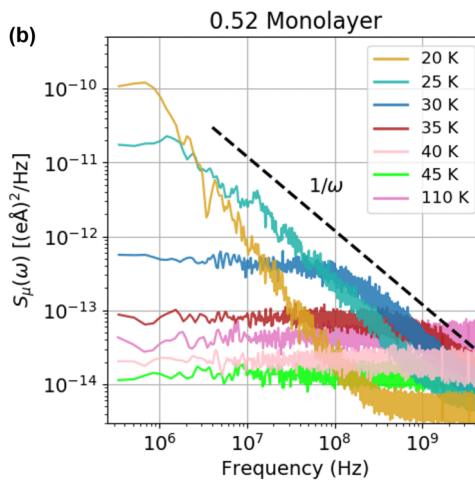
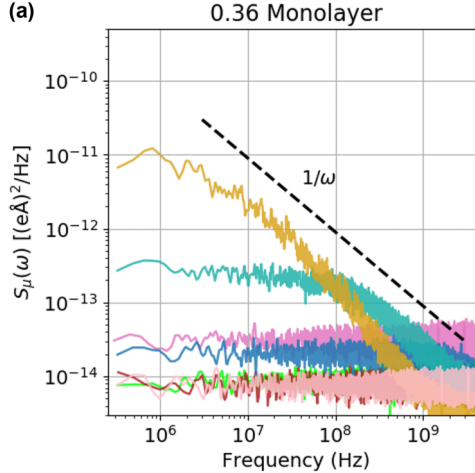


FIG. 20. Individual $S_\mu(\omega)$ spectra obtained from submonolayer coverages over a range of temperatures (analogous to Fig. 4).

up, we would use the following expression:

$$C_{\mu,\mu}(\tau) = \frac{1}{(\mathcal{T} - \tau)} \sum_{k=1}^{\mathcal{T}-\tau} \left[\sum_i^N [\mu_{i,z}(t_k) - \langle \mu_z \rangle] \times [\mu_{i,z}(\tau + t_k) - \langle \mu_z \rangle] \right]. \quad (\text{D2})$$

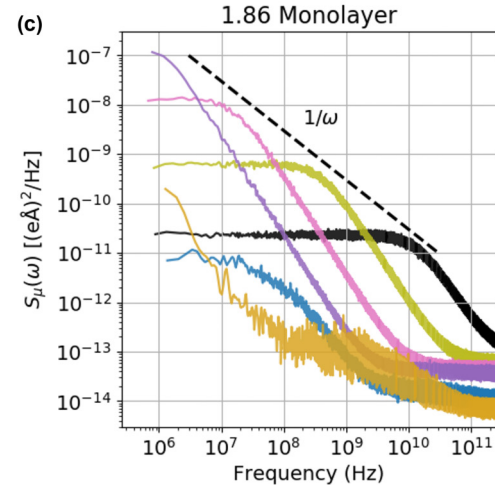
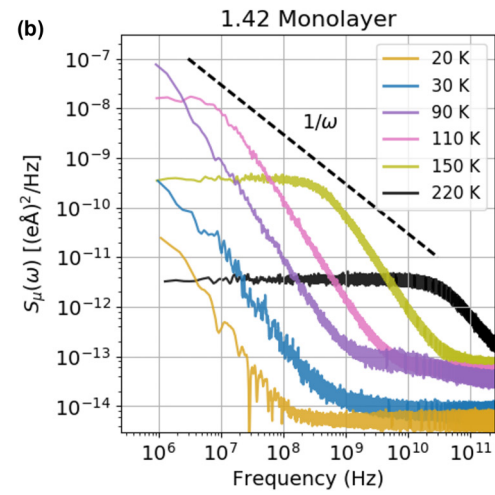
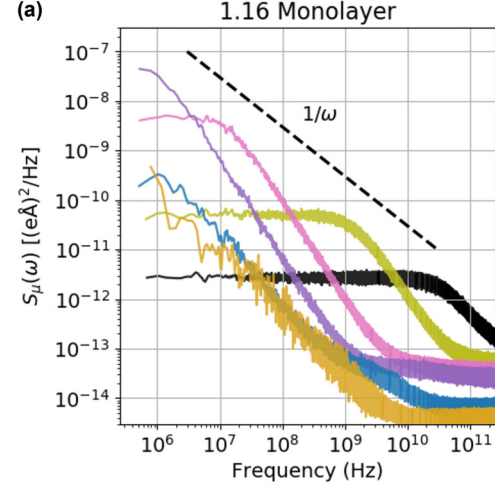


FIG. 21. Individual $S_\mu(\omega)$ spectra obtained from supermonolayer coverages over a range of temperatures (analogous to Fig. 8).

In Eqs. (D1) and (D2), N is the number of particles and \mathcal{T} is the number of time steps used in the simulation. As these equations suggest, another thing to consider is what dipole averages are appropriate to use in these expressions. For the summed case, using the time-averaged summed system dipole is a straightforward choice, but for the individual case there

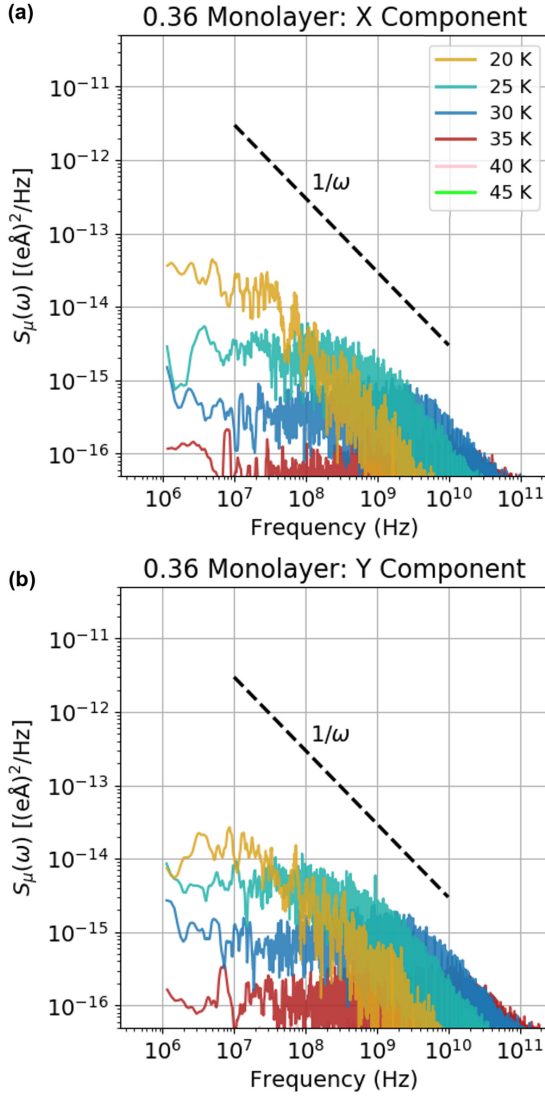


FIG. 22. Spectra obtained from x and y dipole components for 0.36-ML runs. The spectra were smoothed over a window of five time steps.

are several options. We could choose $\langle \mu_z \rangle$ to be the ensemble average of all adsorbate dipoles in the system. Alternatively, we could choose $\langle \mu_z \rangle$ to be an N -length vector composed of N per-particle average dipoles.

To compare the different methods, Figs. 20 and 21 depict dipole-dipole fluctuation spectra of the same trajectories shown in Figs. 4 and 8, respectively, with the individual-style autocorrelation functions used instead of the summed autocorrelation functions (the choice of mean ended up not materially affecting the individual-style spectra very much). Using summed dipole correlation functions results in noisier FT spectra across all trajectories. Differences between the two methods are more apparent in the supermonolayer spectra than the submonolayer spectra. This is primarily because individual-style correlation functions capture *all* layer exchanges, since layer exchanges are individual particle motions, and thus increases how much noise is observed in the supermonolayer spectra where they occur. On the other hand,

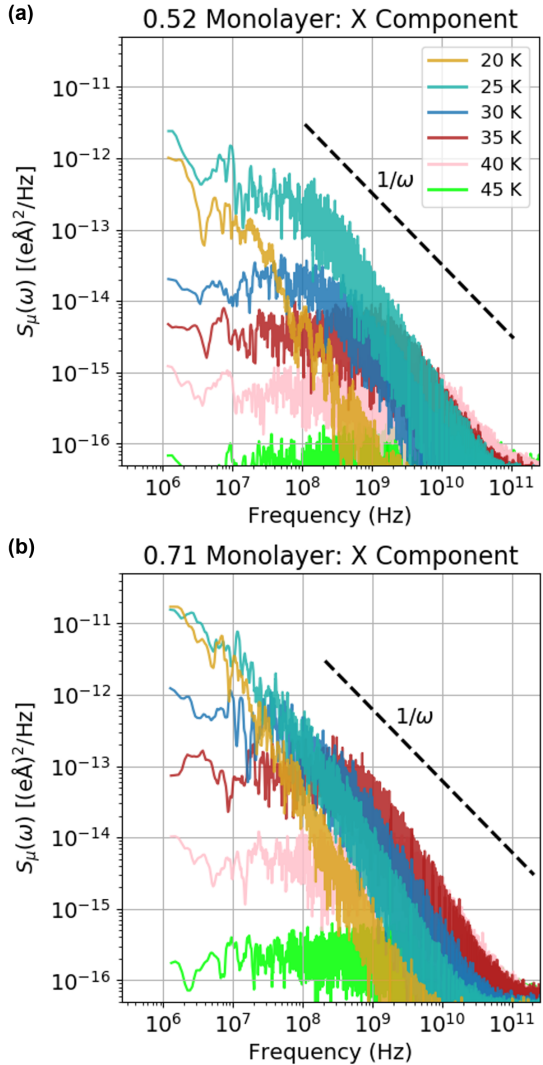


FIG. 23. Spectra obtained from x dipole components from 0.52- and 0.71-ML runs, smoothed over a window of five time steps.

summed correlation functions only capture layer exchanges that result in surface population changes or realignments, which effectively excludes reciprocal layer exchanges.

We decided to use summed autocorrelation functions for the results in the body of the paper. Although noisier, system dipoles are easier to measure experimentally and do not rely on the potentially problematic labeling of indistinguishable particles.

Given that we fixed our system center of mass to reduce drift, it is prudent to be alert for possible small complementary system-wide shifts in response to unidirectional layer exchanges. To head this off, any detected drifts can be corrected for in correlation function calculations. In practice, even if left uncorrected, such shifts would have no effect on summed dipole regime residence times (since they occur at existing events rather than constituting new events) and thus do not affect the frequency scaling or the frequencies at which different features are found in the spectra. Overall magnitudes would only be affected by a small scaling factor (significantly less than one logarithmic unit); this would barely budge the

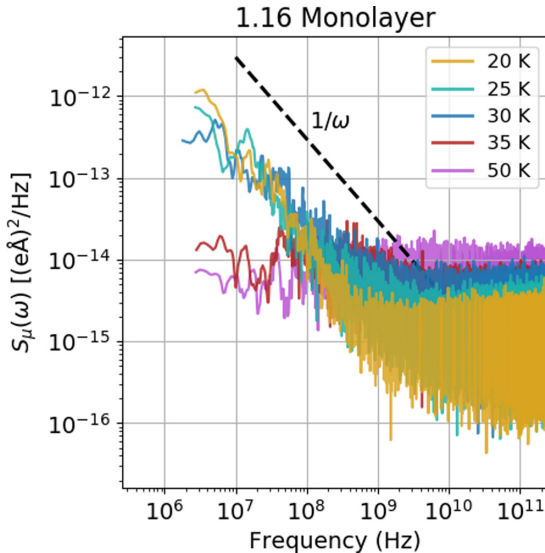


FIG. 24. Selected low-temperature, 1.16-ML $S_\mu(\omega)$ spectra. The spectra were smoothed over a window of five time steps.

positioning of the spectra and is orders of magnitude less than the differences between the spectral trajectories at different temperatures.

- [1] J. Preskill, Quantum computing in the NISQ era and beyond, *Quantum* **2**, 79 (2018).
- [2] D. Wineland, C. Monroe, W. M. Itano, D. Leibfried, B. King, and D. M. Meekhof, Experimental issues in coherent quantum-state manipulation of trapped atomic ions, *J. Res. Natl. Inst. Stand. Technol.* **103**, 259 (1998).
- [3] Q. A. Turchette, Kielpinski, B. E. King, D. Leibfried, D. M. Meekhof, C. J. Myatt, M. A. Rowe, C. A. Sackett, C. S. Wood, W. M. Itano, C. Monroe, and D. J. Wineland, Heating of trapped ions from the quantum ground state, *Phys. Rev. A* **61**, 063418 (2000).
- [4] M. Brownnutt, M. Kumph, P. Rabl, and R. Blatt, Ion-trap measurements of electric-field noise near surfaces, *Rev. Mod. Phys.* **87**, 1419 (2015).
- [5] K. R. Brown, J. Chiaverini, J. M. Sage, and H. Häffner, Materials challenges for trapped-ion quantum computers, *Nat. Rev. Mater.* **6**, 892 (2021).
- [6] C. Wang, C. Axline, Y. Y. Gao, T. Brecht, Y. Chu, L. Frunzio, M. H. Devoret, and R. J. Schoelkopf, Surface participation and dielectric loss in superconducting qubits, *Appl. Phys. Lett.* **107**, 162601 (2015).
- [7] J. M. Martinis, Superconducting phase qubits, *Quantum Inf. Proc.* **8**, 81 (2009).
- [8] D. Lee, J. L. DuBois, and V. Lordi, Identification of the Local Sources of Paramagnetic Noise in Superconducting Qubit Devices Fabricated on $\alpha\text{-Al}_2\text{O}_3$ Substrates Using Density-Functional Calculations, *Phys. Rev. Lett.* **112**, 017001 (2014).
- [9] M. Saffman, Quantum computing with atomic qubits and rydberg interactions: Progress and challenges, *J. Phys. B: At., Mol. Opt. Phys.* **49**, 202001 (2016).
- [10] M. Kim, H. J. Mamin, M. H. Sherwood, K. Ohno, D. D. Awschalom, and D. Rugar, Decoherence of Near-Surface Nitrogen-Vacancy Centers Due to Electric Field Noise, *Phys. Rev. Lett.* **115**, 087602 (2015).
- [11] J. B. Johnson, Thermal agitation of electricity in conductors, *Phys. Rev.* **32**, 97 (1928).
- [12] H. Nyquist, Thermal agitation of electric charge in conductors, *Phys. Rev.* **32**, 110 (1928).
- [13] D. A. Hite, Y. Colombe, A. C. Wilson, D. T. C. Allcock, D. Leibfried, D. J. Wineland, and D. P. Pappas, Surface science for improved ion traps, *MRS Bull.* **38**, 826 (2013).
- [14] H. Häffner, C. F. Roos, and R. Blatt, Quantum computing with trapped ions, *Phys. Rep.* **469**, 155 (2008).
- [15] J. Benhelm, G. Kirchmair, C. F. Roos, and R. Blatt, Towards fault-tolerant quantum computing with trapped ions, *Nat. Phys.* **4**, 463 (2008).
- [16] C. D. Bruzewicz, J. Chiaverini, R. McConnell, and J. M. Sage, Trapped-ion quantum computing: Progress and challenges, *Appl. Phys. Rev.* **6**, 21314 (2019).
- [17] K. C. McCormick, J. Keller, S. C. Burd, D. J. Wineland, A. C. Wilson, and D. Leibfried, Quantum-enhanced sensing of a single-ion mechanical oscillator, *Nature (London)* **572**, 86 (2019).
- [18] C. L. Degen, F. Reinhard, and P. Cappellaro, Quantum sensing, *Rev. Mod. Phys.* **89**, 035002 (2017).
- [19] I. Baumgart, J.-M. Cai, A. Retzker, M. B. Plenio, and C. Wunderlich, Ultrasensitive Magnetometer Using a Single Atom, *Phys. Rev. Lett.* **116**, 240801 (2016).
- [20] D. Leibfried, M. D. Barrett, T. Schaetz, J. Britton, J. Chiaverini, W. M. Itano, J. D. Jost, C. Langer, and D. J. Wineland, Toward

APPENDIX G: x AND y DIPOLE-DIPOLE FLUCTUATION SPECTRA

Figure 22 shows fluctuation spectra using x and y dipole components for the 0.36-ML runs. The difference between using x and y components is quite small for all coverages studied. Figure 23 shows spectra using x dipole components for the 0.52- and 0.71-ML runs. Although for most temperatures the magnitudes of such spectra are quite low, for the lowest of the temperatures for the 0.52- and 0.71-ML runs, the spectra take on large magnitudes that are comparable to or at times exceed the spectra generated from the z dipole values. The x and y dipole-dipole fluctuation spectra show similar features and scalings to the z dipole-dipole fluctuation spectra.

Supermonolayer x and y dipole-dipole fluctuation spectra are not shown: their magnitudes are consistently below those of the spectra from the z dipoles. At the intermediate and high temperatures at which layer exchanges occur, the magnitudes are even lower and the spectra are mostly flat, likely an indication of the key role that out-of-plane rather than in-plane variations play in the noise generated by layer exchanges.

APPENDIX H: LOW-TEMPERATURE SUPERMONOLAYER DIPOLE-DIPOLE FLUCTUATION SPECTRA

Figure 24 shows selected low-temperature, 1.16-ML $S_\mu(\omega)$ spectra. [Higher temperatures are shown in Fig. 8(a)].

- heisenberg-limited spectroscopy with multiparticle entangled states, *Science* **304**, 1476 (2004).
- [21] M. G. Kozlov, M. S. Safronova, J. R. Crespo López-Urrutia, and P. O. Schmidt, Highly charged ions: Optical clocks and applications in fundamental physics, *Rev. Mod. Phys.* **90**, 045005 (2018).
- [22] C. W. Chou, D. B. Hume, J. C. J. Koelemeij, D. J. Wineland, and T. Rosenband, Frequency Comparison of Two High-Accuracy Al⁺ Optical Clocks, *Phys. Rev. Lett.* **104**, 070802 (2010).
- [23] N. Huntemann, C. Sanner, B. Lipphardt, C. Tamm, and E. Peik, Single-Ion Atomic Clock with 3×10^{-18} Systematic Uncertainty, *Phys. Rev. Lett.* **116**, 063001 (2016).
- [24] D. An, C. Matthiesen, E. Urban, and H. Häffner, Distance scaling and polarization of electric-field noise in a surface ion trap, *Phys. Rev. A* **100**, 063405 (2019).
- [25] N. Daniilidis, S. Narayanan, S. A. Moller, R. Clark, T. E. Lee, P. J. Leek, A. Wallraff, S. Schulz, F. Schmidt-Kaler, and H. Häffner, Fabrication and heating rate study of microscopic surface electrode ion traps, *New J. Phys.* **13**, 013032 (2011).
- [26] J. A. Sedlacek, J. Stuart, D. H. Slichter, C. D. Bruzewicz, R. McConnell, J. M. Sage, and J. Chiaverini, Evidence for multiple mechanisms underlying surface electric-field noise in ion traps, *Phys. Rev. A* **98**, 063430 (2018).
- [27] J. A. Sedlacek, A. Greene, J. Stuart, R. McConnell, C. D. Bruzewicz, J. M. Sage, and J. Chiaverini, Distance scaling of electric-field noise in a surface-electrode ion trap, *Phys. Rev. A* **97**, 020302(R) (2018).
- [28] C. Noel, M. Berlin-Udi, C. Matthiesen, J. Yu, Y. Zhou, V. Lordi, and H. Häffner, Electric-field noise from thermally activated fluctuators in a surface ion trap, *Phys. Rev. A* **99**, 063427 (2019).
- [29] J. Labaziewicz, Y. Ge, P. Antohi, D. Leibrandt, K. R. Brown, and I. L. Chuang, Suppression of Heating Rates in Cryogenic Surface-Electrode Ion Traps, *Phys. Rev. Lett.* **100**, 013001 (2008).
- [30] L. Deslauriers, S. Olmschenk, D. Stick, W. K. Hensinger, J. Sterk, and C. Monroe, Scaling and Suppression of Anomalous Heating in Ion Traps, *Phys. Rev. Lett.* **97**, 103007 (2006).
- [31] D. A. Hite, K. S. McKay, S. Kotler, D. Leibfried, D. J. Wineland, and D. P. Pappas, Measurements of trapped-ion heating rates with exchangeable surfaces in close proximity, *MRS Adv.* **2**, 2189 (2017).
- [32] M. Kumph, C. Henkel, P. Rabl, M. Brownnutt, and R. Blatt, Electric-field noise above a thin dielectric layer on metal electrodes, *New J. Phys.* **18**, 023020 (2016).
- [33] M. Teller, D. A. Fioretto, P. C. Holz, P. Schindler, V. Messerer, K. Schüppert, Y. Zou, R. Blatt, J. Chiaverini, J. Sage, and T. E. Northup, Heating of a Trapped Ion Induced by Dielectric Materials, *Phys. Rev. Lett.* **126**, 230505 (2021).
- [34] D. A. Hite, Y. Colombe, A. C. Wilson, K. R. Brown, U. Warring, R. Jördens, J. D. Jost, K. S. McKay, D. P. Pappas, D. Leibfried, and D. J. Wineland, 100-Fold Reduction of Electric-Field Noise in an Ion Trap Cleaned with In Situ Argon-Ion-Beam Bombardment, *Phys. Rev. Lett.* **109**, 103001 (2012).
- [35] N. Daniilidis, S. Gerber, G. Bolloten, M. Ramm, A. Ransford, E. Ulin-Avila, I. Talukdar, and H. Häffner, Surface noise analysis using a single-ion sensor, *Phys. Rev. B* **89**, 245435 (2014).
- [36] K. S. McKay, D. A. Hite, Y. Colombe, R. Jördens, A. C. Wilson, D. H. Slichter, D. T. C. Allcock, D. Leibfried, D. J. Wineland, and D. P. Pappas, Ion-trap electrode preparation with Ne⁺ bombardment, [arXiv:1406.1778](https://arxiv.org/abs/1406.1778).
- [37] R. McConnell, C. Bruzewicz, J. Chiaverini, and J. Sage, Reduction of trapped-ion anomalous heating by in situ surface plasma cleaning, *Phys. Rev. A* **92**, 020302(R) (2015).
- [38] D. T. C. Allcock, L. Guidoni, T. P. Harty, C. J. Ballance, M. G. Blain, A. M. Steane, and D. M. Lucas, Reduction of heating rate in a microfabricated ion trap by pulsed-laser cleaning, *New J. Phys.* **13**, 123023 (2011).
- [39] A. Safavi-Naini, P. Rabl, P. F. Weck, and H. R. Sadeghpour, Microscopic model of electric-field-noise heating in ion traps, *Phys. Rev. A* **84**, 023412 (2011).
- [40] A. Safavi-Naini, E. Kim, P. F. Weck, P. Rabl, and H. R. Sadeghpour, Influence of monolayer contamination on electric-field-noise heating in ion traps, *Phys. Rev. A* **87**, 023421 (2013).
- [41] K. G. Ray, B. M. Rubenstein, W. Gu, and V. Lordi, Van der waals-corrected density functional study of electric field noise heating in ion traps caused by electrode surface adsorbates, *New J. Phys.* **21**, 053043 (2019).
- [42] P. Dutta and P. M. Horn, Low-frequency fluctuations in solids: 1/f noise, *Rev. Mod. Phys.* **53**, 497 (1981).
- [43] N. Zanolla, Characterization and Modeling of Low-Frequency Noise in MOSFETs, Ph.D. thesis, University of Bologna, 2009.
- [44] M. B. Weissman, 1/f noise and other slow, nonexponential kinetics in condensed matter, *Rev. Mod. Phys.* **60**, 537 (1988).
- [45] E. Kim, A. Safavi-Naini, D. A. Hite, K. S. McKay, D. P. Pappas, P. F. Weck, and H. R. Sadeghpour, Electric-field noise from carbon-adatom diffusion on a Au(110) surface: First-principles calculations and experiments, *Phys. Rev. A* **95**, 033407 (2017).
- [46] H. Jooya, K. McKay, E. Kim, P. Weck, D. Pappas, D. Hite, and H. Sadeghpour, Mechanisms for carbon adsorption on Au(110)-(2 × 1): A work function analysis, *Surf. Sci.* **677**, 232 (2018).
- [47] R. Dubessy, T. Coudreau, and L. Guidoni, Electric field noise above surfaces: A model for heating-rate scaling law in ion traps, *Phys. Rev. A* **80**, 031402(R) (2009).
- [48] F. Rossi and G. I. Opat, Observations of the effects of adsorbates on patch potentials, *J. Phys. D: Appl. Phys.* **25**, 1349 (1992).
- [49] G. Kresse and J. Furthmüller, Efficient iterative schemes for ab initio total-energy calculations using a plane-wave basis set, *Phys. Rev. B* **54**, 11169 (1996).
- [50] K. Berland and P. Hyldgaard, Exchange functional that tests the robustness of the plasmon description of the van der waals density functional, *Phys. Rev. B* **89**, 035412 (2014).
- [51] W. L. Jorgensen, J. D. Madura, and C. J. Swenson, Optimized intermolecular potential functions for liquid hydrocarbons, *J. Am. Chem. Soc.* **106**, 6638 (1984).
- [52] A. L. Hjorth, J. J. Mortensen, J. Blomqvist, I. E. Castelli, R. Christensen, M. Dułak, J. Friis, M. N. Groves, B. Hammer, C. Hargus *et al.*, The atomic simulation environment – a python library for working with atoms, *J. Phys.: Condens. Matter* **29**, 273002 (2017).
- [53] <https://www.github.com/blfoulon/ion-trap-anomalous-heating-simulation/>.
- [54] W. H. Press and G. B. Rybicki, Fast algorithm for spectral analysis of unevenly sampled data, *Astrophys. J.* **338**, 277 (1989).
- [55] R. B. Blackman and J. W. Tukey, The measurement of power spectra from the point of view of communications engineering – Part I, *Bell Syst. Tech. J.* **37**, 185 (1958).

- [56] S. Machlup, Noise in semiconductors: Spectrum of a two-parameter random signal, *J. Appl. Phys.* **25**, 341 (1954).
- [57] H. Z. Jooya, X. Fan, K. S. McKay, D. P. Pappas, D. A. Hite, and H. R. Sadeghpour, Crystallographic orientation dependence of work function: Carbon adsorption on Au surfaces, *Mol. Phys.* **117**, 2157 (2019).
- [58] J. J. Shynk, *Probability, Random Variables, and Random Processes: Theory and Signal Processing Applications* (Wiley, Hoboken, NJ, 2012).